

PAPER

Modal kinematics for multisection continuum arms

To cite this article: Isuru S Godage *et al* 2015 *Bioinspir. Biomim.* **10** 035002

View the [article online](#) for updates and enhancements.

Related content

- [Bioinspired locomotion and grasping in water: the soft eight-arm OCTOPUS robot](#)
M Cianchetti, M Calisti, L Margheri *et al.*
- [Design, modeling and control of a pneumatically actuated manipulator inspired by biological continuum structures](#)
Rongjie Kang, David T Branson, Tianjiang Zheng *et al.*
- [A bioinspired soft manipulator for minimally invasive surgery](#)
T Ranzani, G Gerboni, M Cianchetti *et al.*

Recent citations

- [Shape-based coordination in locomotion control](#)
Matthew Travers *et al*
- [Dynamic Modeling of a Class of Continuum Manipulators in Fixed Orientation](#)
Ammar Amouri *et al*

Bioinspiration & Biomimetics



SPECIAL ISSUES/SECTIONS

Modal kinematics for multisection continuum arms

Isuru S Godage¹, Gustavo A Medrano-Cerda², David T Branson³, Emanuele Guglielmino² and Darwin G Caldwell²

¹ Department of Electrical and Computer Engineering, Clemson University, Clemson, SC 29634, USA

² Department of Advanced Robotics, Istituto Italiano di Tecnologia, Via Morego 30, I-16163 Genoa, Italy

³ Mechanical, Materials and Manufacturing Department, University of Nottingham, NG7 4HS, UK

E-mail: igodage@g.clemson.edu

Keywords: continuum arms, modal shape functions, inverse kinematics, redundant manipulators, kinematic decoupling

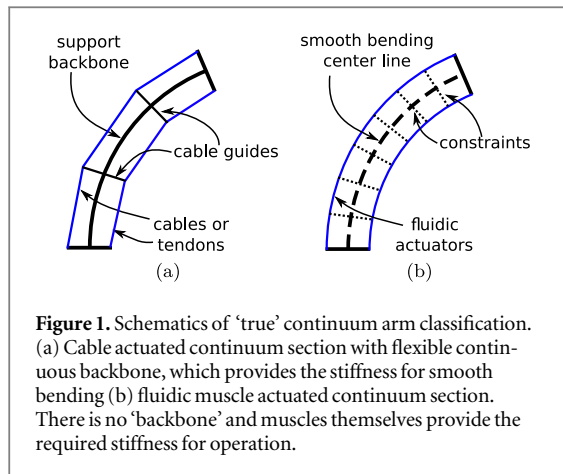
Abstract

This paper presents a novel spatial kinematic model for multisection continuum arms based on mode shape functions (MSF). Modal methods have been used in many disciplines from finite element methods to structural analysis to approximate complex and nonlinear parametric variations with simple mathematical functions. Given certain constraints and required accuracy, this helps to simplify complex phenomena with numerically efficient implementations leading to fast computations. A successful application of the modal approximation techniques to develop a new modal kinematic model for general variable length multisection continuum arms is discussed. The proposed method solves the limitations associated with previous models and introduces a new approach for readily deriving exact, singularity-free and unique MSF's that simplifies the approach and avoids mode switching. The model is able to simulate spatial bending as well as straight arm motions (i.e., pure elongation/contraction), and introduces inverse position and orientation kinematics for multisection continuum arms. A kinematic decoupling feature, splitting position and orientation inverse kinematics is introduced. This type of decoupling has not been presented for these types of robotic arms before. The model also carefully accounts for physical constraints in the joint space to provide enhanced insight into practical mechanics and impose actuator mechanical limitations onto the kinematics thus generating fully realizable results. The proposed method is easily applicable to a broad spectrum of continuum arm designs.

1. Introduction

Continuum robotic arm research has made significant progress in recent times (Walker 2013). There have been many prototypes proposed over the years for various applications and they successfully proved their versatility in field applications (McMahan *et al* 2006). Continuum arms can be realized utilizing different actuation technologies such as tendons/cables (Gravagne and Walker 2000), fluidic (pneumatic or hydraulic) muscle actuators (Grissom *et al* 2006), shape memory alloys (Seok *et al* 2013, Laschi *et al* 2012) among others. A continuum section is usually actuated with three actuators, which is the optimal actuator configuration for spatial operation, although other combinations (Zheng *et al* 2013, Maz-zolai *et al* 2012) are possible. Out of these, tendon driven continuous backbone or fluidic muscle

actuated 'true' continuum arms (Robinson and Davies 1999), as shown in figure 1, offer promising prospects for wide range of applications such as minimally invasive surgeries (Conrad *et al* 2013, Xu K and Simaan 2010), underwater operations (Davies *et al* 1998), object grasping/manipulation (Li and Xiao 2011), and legged locomotion (Suzumori 1996, Godage *et al* 2012b). Figure 2 shows two pneumatic muscle actuator (PMA) powered multisection continuum arms. PMA's are particularly suitable for implementing multisection continuum arms owing to their high flexibility and power to weight ratio (Caldwell *et al* 1995). Unfortunately, the modeling of continuum arms, particularly dynamic modeling, has been lagging with many open research problems such as lack of kinematic decoupling and numerically stable spatial dynamic models (Trivedi *et al* 2008).

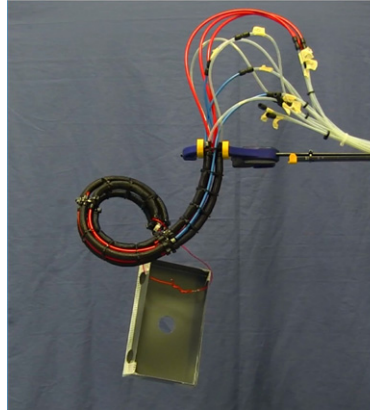


Discrete continuum robotic arms (Buckingham 2002) are high degree of freedom (DOF) serial rigid-link implementations and therefore the mathematical modeling was unambiguous as rigid links are assumed to undergo no deformation. Continuum robotic arms on the other hand represents a flexible ‘invertebrate’ structure and are subject to significant deformation during operation making the mathematical modeling complicated. This is particularly true in dynamic modeling where continuum robots have to solely rely on energy based models to derive equations of motions. Whereas rigid-body based robots can benefit from the efficient algorithms such as recursive Newton–Euler Dasgupta and Choudhury (1999) or spatial dynamics Featherstone (2008). Lumped approximation methods (Zheng *et al* 2012, Giri and Walker 2011, Mahl *et al* 2012) mark the natural evolution from the rigid-linked to continuum arm modeling but have certain limitations. They require many virtual discrete rigid-link segments to accurately resemble a continuum arm thus markedly increasing the overall DOF in contrast to de facto joint variables. This poses computational problems particularly for computing inverse kinematic solutions employing iterative methods. Parametric representations avoid these problems by describing kinematics with shape functions to accommodate continuous smooth bending.

In rigid bodies, the displacement between any two points remains unchanged and therefore the body’s spatial location (position and orientation) can be completely described with six DOF with respect to a fixed reference frame. However, in deformable bodies the displacement between points vary during operation and to completely define spatial location, each point must be represented separately. Thus an infinite number of DOF’s are required. For instance, in the continuum arm section shown in figure 3, two deformation paths ($\{A1, B1\}$ and $\{A2, B2\}$) out of an infinite number of possibilities are illustrated for points A and B on the neutral axis of the undeformed body. The displacement of these points with respect to their undeformed position can be mathematically

expressed using a parametric displacement field which can account for any kinematic constraint governing the body deformation. These displacement fields are usually in the form of spatial curves (or similar parameterization) or multivariate polynomials of joint space variables. This is the basis of the modal approach for kinematics of deformable continuum arms.

Kinematic models employing modal approaches have been proposed for continuum style robots to simplify the variation of position and orientation during operation. Chirikjian and Burdick (1994) proposed a general modal method for complex ‘hyper-redundant’ extensible robotic structures using parametric integral shape functions. With this spatial model it was possible to study motion planning (Chirikjian and Burdick 1990a), analyze/implement locomotion (Burdick *et al* 1993), and other tasks/behaviors that are unique to hyper-redundant robots. Mochiyama (2006) proposed a kinematic model for hyper-flexible bodies with one-dimensional topological structure. The particular curves that were chosen (often derivative of the Frenet–Surret frames) had no configuration resemblance to the actual robot. Additionally these robots were essentially high DOF rigid bodied robots which can be efficiently and accurately modeled with conventional rigid body kinematics and dynamics. But the use of MSF’s simplified the number of parameters to vary (i.e., kinematic DOF) to speed up the kinematic and dynamic computations employing then available technology. However these shape parameterizations constrains a particular robot to an ‘application specific’ and ‘reduced’ set of shapes and/or motions. This may require complete redefining of the shape functions for different applications or requirements. Occasionally a single shape function is not adequate to depict the parameter variation within the range of entire task-space therefore requiring several overlapping shape functions resulting in mode switching and complicated error models. Also, the use of additional transformations to fit the different morphologies to shape functions in previous approaches can pose nonlinear parameter mapping problems, discontinuities, and modal singularities. Moreover, the shape functions do not resemble the actual structure of the robot and gives limited practical insight to understand the internal mechanism. Consequently, it is difficult to impose actuator constraints such as the length change limits. Unless there exists a complete mapping between shape parameters and joint space variables, results of these models cannot be applicable to spatial continuum or hyper-redundant robots. Further, there is no straightforward method to determine these MSF’s. Shabana (2005) employed shape functions to model the deformation of flexible multibody systems. Therein the position displacement field, $u_x \in \mathbb{R}^3$ was denoted by an infinite series of elastic coordinates as



(a)



(b)

Figure 2. Pneumatic muscle actuated state of the art multisection continuum arms. (a) Three-section continuum robotic arm prototype developed in Istituto Italiano di Tecnologia (Italian Institute of Technology), Genova, Italy. (b) Three continuum-section OctArm V robotic arm (courtesy of Ian Walker of Clemson university, Clemson, USA).

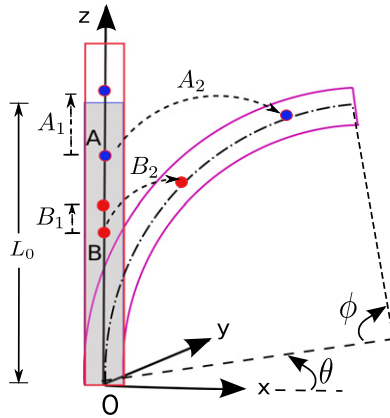


Figure 3. Displacement field of a continuum body with relative displacement of two points due to body deformations.

$$u_x = \alpha_1 f_1 + \alpha_2 f_2 + \alpha_3 f_3 + \alpha_4 f_3 \dots = \sum_{k=1}^{\infty} \alpha_k f_k, \quad (1)$$

where f_k are the elastic coordinates which are functions of joint space variables and $\alpha_k \in \mathbb{R}^3$ are numerical coefficients that define the shape of the displacement field.

Because of computational difficulties associated with infinite dimensional spaces often resulting in partial differential equations, the displacement is generally approximated to a finite number of elastic coordinates to meet any user specified accuracy. However this method assumes that the relative deformation is quantitatively small in comparison to actual dimensions. Hence the displacement field can be approximated to simple multivariate polynomials which could be experimentally identified through simple curve fitting techniques. But continuum arm sections can exhibit omni-directional bending over 180° thus contributing to large deformations in both

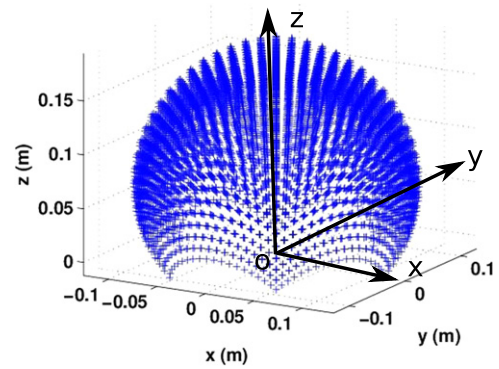


Figure 4. The kinematic workspace for a single continuum section.

position and orientation. A typical kinematic workspace of a single continuum section is illustrated in figure 4. As a result the deformation of continuum arms cannot be approximated with simple shape functions.

The curve parametric (CP) kinematic model by Jones and Walker (2006) remains the state of the art for multisection continuum robotic arms and produces correct and structurally accurate forward kinematics and linear position inverse kinematics via iterative methods. It can model any ‘true’ continuum arm that undergoes linear and/or bending deformation with other actuator configurations. Unlike lumped models, it compactly represents the smooth bending in the actual joint space variables (i.e., actuator lengths) and therefore yields fast results and gives a better physical interpretation. Also it inspired many other similar kinematic models (Baillly *et al* 2011, Rolf and Steil 2012) and provided the analytical foundation for related studies of continuum arms (Braganza *et al* 2006, Kapadia *et al* 2010). Along with these advantages, there are however some limitations to this

model. It cannot model straight arm poses (pure elongations or contractions when actuator lengths are equal) of continuum sections owing to a numerical singularity. Also the results within the singularity neighborhood are unreliable and this particularly affects the iterative inverse kinematic solutions. Moreover, deriving equations of motion for continuum arms results in complex nonlinear integrals which are computationally infeasible in addition to the inherent numerical instabilities (Tatlcioglu et al 2007). Nepalli et al (2009) proposed a closed form inverse kinematic solution for multisection continuum arms but the model only accounts for distance constraints between continuum sections whereas the position and orientation are strictly mechanically coupled. Additionally, the kinematics is expressed in curve parameters without accounting for the geometrical constraints between them. This could yield solutions with CP combinations that cannot be translated to physically realizable joint space variables, i.e., actuator lengths. Further, there are at this time no orientation inverse kinematic models proposed for multisection continuum arms. These limitations critically affect the modeling of potential applications such as whole arm manipulation and object inspection where the kinematic decoupling feature is important for making use of its dexterous behavior. An elaborated account of these drawbacks will be presented in section 2.

Considering these limitations, a novel kinematic model for multisection continuum arms is required and presented here. The method attempts to combine the structural accuracy of the CP kinematics and numerical efficiency of modal methods to develop a novel modal kinematic model. It circumvents the kinematic singularities in CP models and introduces orientation inverse kinematics of multisection continuum arms previously not demonstrated in the literature. The method facilitates intuitive derivation of MSF's which could be functionally implemented for recursive usage for all the continuum sections of the arm. The numerical stability of the model results in efficient iterative solutions directly in the joint space without using intermediary transformations or curve parameters. Hence the model provides enhanced insight into the practical mechanics of the robotic arm. The proposed model is also easily extended to any geometrically constrained variable length multisection continuum arm of any actuator configuration.

The organization of this paper is as follows. First in section 2 the curve CP model is derived and its limitations discussed in detail to highlight the need for an alternative approach to modeling multisection continuum arm kinematics. Section 3 describes the MSF based approach for a single continuum arm section. This is then extended and generalized to multisection continuum arms in section 4 which is verified by simulation and experimental results in section 5, followed by conclusions in section 6.

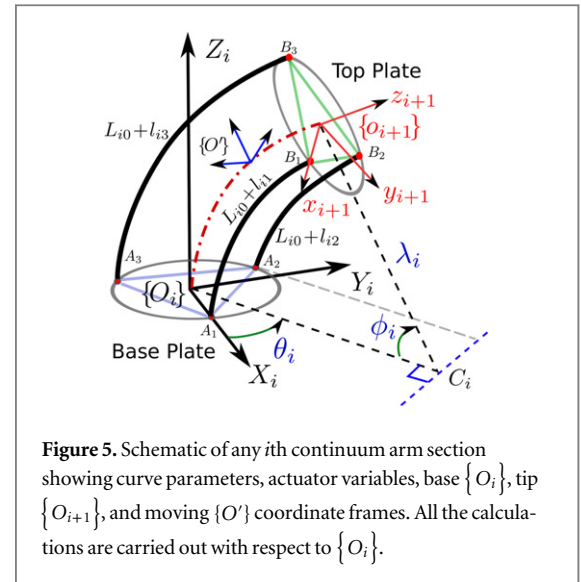


Figure 5. Schematic of any i th continuum arm section showing curve parameters, actuator variables, base $\{O_i\}$, tip $\{O_{i+1}\}$, and moving $\{O'\}$ coordinate frames. All the calculations are carried out with respect to $\{O_i\}$.

2. Curve parametric kinematics and limitations

In this section, the curve parameters that define the spatial orientation of a general single continuum arm section are derived. Afterwards the forward kinematic for a single continuum arm section is derived. The limitations of CP kinematics are then illustrated with exemplary numerical solutions for forward and inverse kinematic problems.

2.1. System model

The multisection continuum robotic arm, for which the modal kinematics was originally developed, is shown in figure 2(a). It has three continuum sections consisting of three mechanically identical extending PMA's each. Consider the schematic of any i th section of a multisection continuum arm as shown in figure 5. Without losing generality, the three variable length actuator configuration is considered and the actuators are fixed to a circular rigid frame at a radius r_i from the center and $\frac{2\pi}{3}$ rads apart. They are mechanically constrained to actuate at a distance r_i parallel to the neutral axis, a hypothetical line running through the center along the length of the continuum section. The actuator original length is L_{i0} and length variation $l_{ij} \in \mathbb{R}$ where $l_{i:\min} \leq l_{ij}(t) \leq l_{i:\max}$, i is the continuum section number, $j \in \{1, 2, 3\}$ is the actuator number, and t is the time. The lower and upper bounds of the length change are $l_{i:\min} \in \mathbb{R}_0^-$ and $l_{i:\max} \in \mathbb{R}_0^+$ respectively. In this way, both extending ($l_{i:\min} = 0, 0 \leq l_{i:\max}$) and contracting ($l_{i:\min} \leq 0, l_{i:\max} = 0$) actuators (i.e., tendons) can be accounted for. The length of an actuator at any time is then $L_{ij}(t) = L_{i0} + l_{ij}(t)$. Note that $L_{i0} > 0$ and $r_i > 0$ are design parameters of continuum sections and are known constants. The joint variable vector for the i th section is $q_i = [l_{i1}(t) \ l_{i2}(t) \ l_{i3}(t)]^T \in \mathbb{R}^3$.

2.2. Curve parameters and forward kinematics

Due to the constrained actuator arrangement, upon actuation these continuum sections either exhibit pure straight arm movements (extend or contract) or bend in a circular arc shape. Therefore the spatial orientation of a continuum section can be completely described (under the assumption of no excessive external loading) as a circular arc with variable curvature radius and length. The arc is defined by three spatial parameters; radius of curvature $\lambda_i \in (0, \infty)$ with instantaneous center C_i , angle subtended by the bending arc $\phi_i \in [0, 2\pi_{\max})$, and angle of the bending plane with respect to the $+X_i$ axis (i.e., O_iX_i and O_iC_i), $\theta_i \in [-\pi, \pi]$. Previous works employed lengthy procedures to derive these parameters in joint variables, but a simpler and straightforward geometrical approach is detailed in appendix A.1. The curve parameters in joint space variables are

$$\begin{aligned}\lambda_i(q_i) &= \frac{(3L_{i0} + l_{i1} + l_{i2} + l_{i3})r_i}{2\sqrt{l_{i1}^2 + l_{i2}^2 + l_{i3}^2 - l_{i1}l_{i2} - l_{i1}l_{i3} - l_{i2}l_{i3}}} \\ \phi_i(q_i) &= \frac{2\sqrt{l_{i1}^2 + l_{i2}^2 + l_{i3}^2 - l_{i1}l_{i2} - l_{i1}l_{i3} - l_{i2}l_{i3}}}{3r_i} \\ \theta_i(q_i) &= \tan^{-1}\left(\frac{\sqrt{3}(l_{i3} - l_{i2})}{l_{i2} + l_{i3} - 2l_{i1}}\right).\end{aligned}\quad (2)$$

The curve parameters have important design implications. One can calculate the r_i required to achieve a desired maximum bending angle ($\phi_{i:\max}$) for given variable length actuators. For instance, contracting PMA's have less actuation range than that of extending ones (Walker et al 2006). Therefore to obtain the same $\phi_{i:\max}$ using PMA's with the same L_{i0} , r_i of the contracting PMA actuated continuum section needs to be shorter. Similarly, other mechanical parameters such as L_{i0} , can also be calculated according to user specifications which are essential for choosing suitable commercial PMA's.

For complete kinematic modeling both position and orientation must be correctly calculated. Because of the large inherent mechanical deformation, continuum sections have varying orientation along the length which has to be represented with a continuous homogeneous transformation matrix (HTM). Therefore a moving coordinate frame $\{O'\}$ is defined (see figure 5) and a scalar parameter $\xi_i \in [0, 1]$ is also introduced to move $\{O'\}$ from the base ($\xi_i = 0$) to the tip ($\xi_i = 1$) along the neutral axis. This work only uses homogeneous translational and rotational transformations based on curve parameters to efficiently derive the accurate HTM. The proposed method is detailed in appendix A.2 and the resulting CP HTM of the i th continuum section, $T_i^c \in SE(3)$, is given by

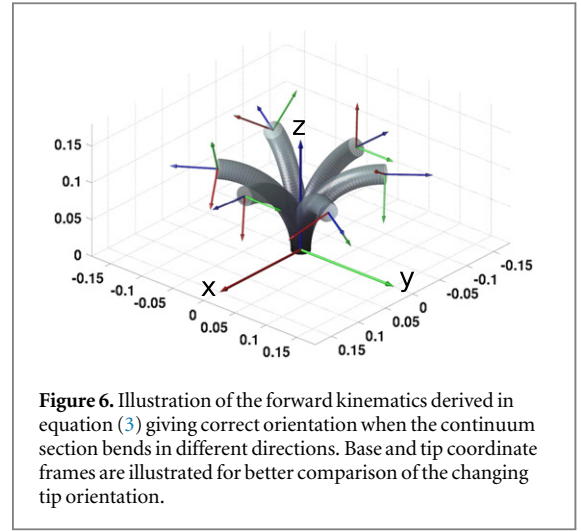


Figure 6. Illustration of the forward kinematics derived in equation (3) giving correct orientation when the continuum section bends in different directions. Base and tip coordinate frames are illustrated for better comparison of the changing tip orientation.

$$T_i^c(c_i, \xi_i) = \begin{bmatrix} R_i^c(c_i, \xi_i) & p_i^c(c_i, \xi_i) \\ \mathbf{0}_{1 \times 3} & 1 \end{bmatrix}, \quad (3)$$

where $c_i = [\lambda_i, \phi_i, \theta_i]^T \in \mathbb{R}^3$ is the curve parameter vector, $R_i^c \in SO(3)$, $p_i^c = [x_i^c, y_i^c, z_i^c]^T \in \mathbb{R}^3$ are the rotational and translational matrices of the respective i th continuum section and

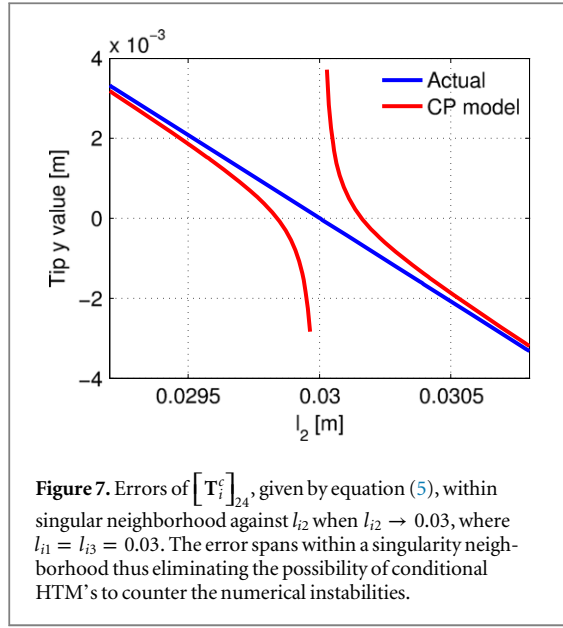
$$\begin{aligned} [R_i^c]_{11} &= \cos^2 \theta_i \cos(\xi_i \phi_i) + \sin^2 \theta_i \\ [R_i^c]_{12} &= \cos \theta_i \sin \theta_i (\cos(\xi_i \phi_i) - 1) \\ [R_i^c]_{13} &= \cos \theta_i \sin(\xi_i \phi_i), \quad [R_i^c]_{21} = [R_i^c]_{12} \\ [R_i^c]_{22} &= \sin^2 \theta_i \cos(\xi_i \phi_i) + \cos^2 \theta_i \\ [R_i^c]_{23} &= \sin \theta_i \sin(\xi_i \phi_i) \\ [R_i^c]_{31} &= -[R_i^c]_{13}, \quad [R_i^c]_{32} = -[R_i^c]_{23} \\ [R_i^c]_{33} &= \cos(\xi_i \phi_i) \\ [p_i^c]_1 &= \lambda_i \cos \theta_i (1 - \cos(\xi_i \phi_i)) \\ [p_i^c]_2 &= \lambda_i \sin \theta_i (1 - \cos(\xi_i \phi_i)), \\ [p_i^c]_3 &= \lambda_i \sin(\xi_i \phi_i). \end{aligned}$$

Figure 6 shows how the continuum arm section produces the correct tip orientation as the arm bends toward different directions.

2.3. Limitations of CP kinematics

In this section, the limitations of the CP kinematics are exemplified with numerical examples. The knowledge obtained by doing so is then employed to circumvent those limitations in the proposed modal kinematics.

In a singular condition when all actuator lengths are equal, the denominator and numerator become zero in all terms having θ_i and λ_i rendering them undefined. Consider the matrix element $[T_i^c]_{24}$ given in curve parameters by equation (4), and subsequently



derived in joint space variables as

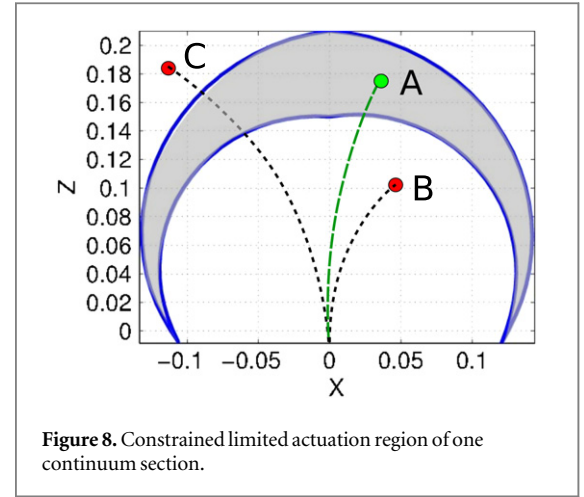
$$\left[\mathbf{T}_i^c(\mathbf{q}_i, \xi_i) \right]_{24} = \lambda_i \sin \theta_i \left\{ 1 - \cos(\xi_i \phi_i) \right\} \quad (4)$$

$$= \frac{\sqrt{3} (l_{i2} - l_{i3}) (3 L_{i0} + l_{i1} + l_{i2} + l_{i3}) r_i}{4u^2} \left\{ \cos(2\xi_i u / 3r_i) - 1 \right\}, \quad (5)$$

where $u = \sqrt{l_{i1}^2 + l_{i2}^2 + l_{i3}^2 - l_{i1}l_{i2} - l_{i1}l_{i3} - l_{i2}l_{i3}}$.

Figure 7 shows the numerical error when all length variables are approaching the same value, i.e., $l_{i3} \rightarrow l_{i1} = l_{i2} = 0.03$ m. Also the error of $\left[\mathbf{T}_i^c \right]_{24}$ spans a range within the significantly large errors which would yield unreliable results across the singularity neighborhood. Hence simple limiting case HTM substitutions at singular conditions reported in (Rolf and Steil 2012) do not circumvent this problem thus motivating a generalized solution.

To elaborate the limitations related to inverse kinematics, consider an extending PMA operated ($l_{i:\min} = 0$, $l_{i:\max} = 0.06$ m) multisection continuum arm similar to figure 2(a). Hence the length of individual continuum sections can only increase during operation. Because of the kinematic redundancy, position inverse kinematics can be solved iteratively (Jones and Walker 2006). However, the Jacobian also inherits the numerical instabilities of the HTM listed by equation (3) and yields large errors within singular neighborhoods. For multisection continuum arms this increases the probability of numerical problems as any continuum section close to singularities would cause inaccuracies in the overall outcome. Further, the use of curve parameters without joint space constraints and coupling lead to inaccurate inverse kinematic solutions. For instance, consider the inverse relationship between l_{i1} and curve parameters of equation (A.2) given by



$$l_{i1} = \left\{ \lambda_i - r_i \cos(\theta_i) \right\} \phi_i - L_{i0}.$$

Not only is there no means to impose the correlation of the curve parameters but other apparent problems also arise such as producing the same result for both θ_i and $-\theta_i$, which cannot be constrained as $\theta_i \in [-\pi, \pi]$. The shaded region in figure 8 shows the physically realizable arm tip locations of a single continuum section on the $y = 0$ plane. Thus, for curve parameters corresponding to any point within the shaded region (i.e., point A) a realizable inverse kinematic solution exists. For points outside (i.e., points B and C) the solutions calculated as feasible using current methods but are impossible for a given arm section to realize. This phenomenon can be further emphasized by solving for position inverse kinematics utilizing multisection continuum arm CP kinematics. Figure 9 shows a couple of CP inverse kinematic solutions to the desired task-space position $\mathbf{p}_t = [0.3, 0.3, 0.3]^T$ using the iterative Newton–Raphson method. In figure 9(a), the third continuum section is extended beyond its mechanical capabilities. The base and mid sections are contracted which is not possible with extending PMA's. Similarly, in figure 9(b) only the third section produces a realizable solution while the rest is not implementable. The modal kinematics for continuum arms solve these issues and are discussed next.

3. Modal approach for continuum arm kinematics

This section presents the new approach to model position and orientation of a single continuum section in modal form. Note that, because of the structural inaccuracies associated with the prior arbitrary MSF models, the accuracy and performance results of the proposed MSF will be compared only to the state of the art CP model by Jones and Walker (2006).

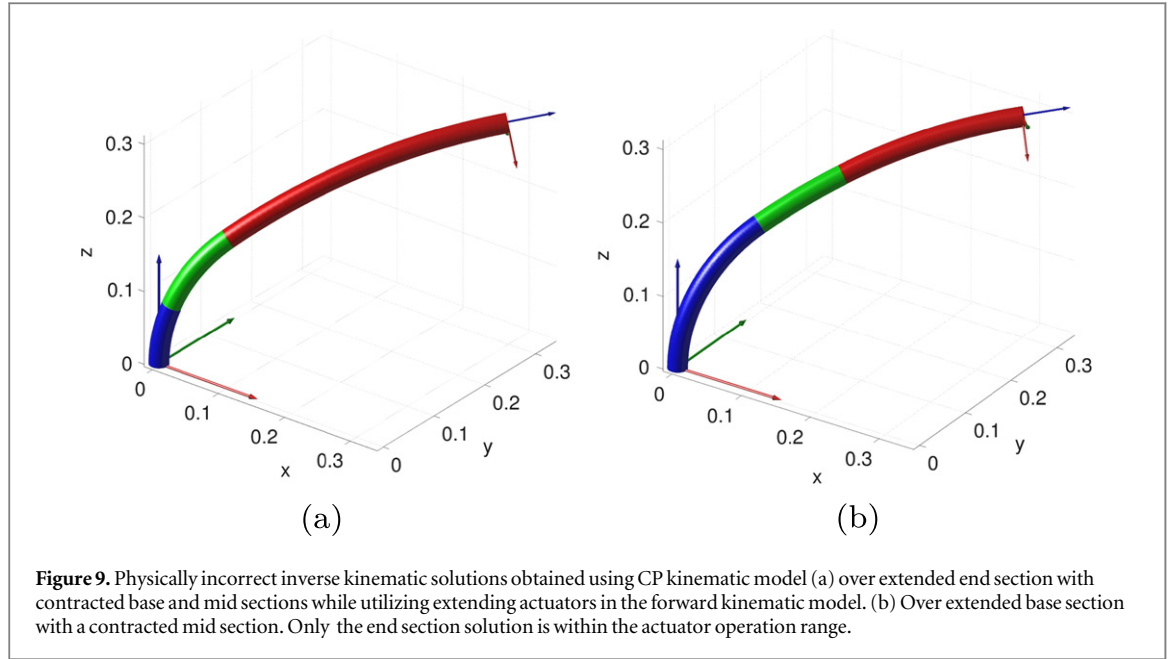


Figure 9. Physically incorrect inverse kinematic solutions obtained using CP kinematic model (a) over extended end section with contracted base and mid sections while utilizing extending actuators in the forward kinematic model. (b) Over extended base section with a contracted mid section. Only the end section solution is within the actuator operation range.

3.1. Deriving mode shape functions

The intuitive approach is to represent rotational and position components of the HTM, given in equation (3), in modal form as $[T_i^c]_{jk} = f_{jk}(l_{i1}, l_{i2}, l_{i3})$ similar to equation (1) where $[T_i^c]_{jk}$ are any j -row and k -column element of T_i^c . The typical modal approaches employ low order polynomial approximations (Shabana 1998) or parametric curves (Chirikjian and Burdick 1990b). However, in order to retain the physical insight and avoid nonlinear mapping problems, MSF are preferred to retain joint space representation. An alternative way of deriving MSF's is through curve fitting position and orientation components. But multi-dimensional curve fitting over the parameter ranges of continuum arms is computationally demanding and yields poor results. Therefore a simple and straightforward alternative is required for finding suitable MSF's to describe the deformation field of continuum arms.

The CP HTM given by equation (3) already encompasses the position and orientation of a continuum section in joint space. The singularity problem can be circumvented if the entries in the HTM are approximated to numerically stable multivariate polynomials. Different types of series expansions methods, such as power, Fourier and Taylor series (Adams and Essex 2006) are available for simplifying complex nonlinear functions. Especially considering the task at hand, the multivariate Taylor series expansion produces polynomial terms without trigonometric terms or denominators having joint variables and hence effectively removes the numerical instabilities. Therefore the MSF approximations for the CP HTM elements are obtained by applying multivariate Taylor series expansion for joint variables, l_{i1} , l_{i2} , and l_{i3} at $\mathbf{0}$ and the result is the modal HTM, $T_i \in SE(3)$ given by

$$T_i(q_i, \xi_i) = \begin{bmatrix} R_i(q_i, \xi_i) & p_i(q_i, \xi_i) \\ \mathbf{0}_{1 \times 3} & 1 \end{bmatrix}, \quad (6)$$

where $R_i \in SO(3)$ and $p_i \in \mathbb{R}^3$ are respectively the modal rotation matrix and modal position vector along the neutral axis. This produces multivariate polynomials having positive exponent-joint variable terms for each HTM element that can be easily derived by built-in subroutines such as 'taylor' or 'mtaylor' of symbolic computer algebra systems SAGEMATH® (Stein et al 2012) or Maplesoft (2009)® respectively. For instance, the MSF of $[T_i]_{24} \in \mathbb{R}$ is given by

$$[T_i(q_i, \xi_i)]_{24} = \sqrt{3} (3 L_{i0} + l_{i1} + l_{i2} + l_{i3}) (l_{i2} - l_{i3}) \left(\frac{-\xi_i^2}{18r_i} + \frac{u^2 \xi_i^4}{486r_i^3} + \frac{u^4 \xi_i^6}{32805r_i^5} + \dots \right), \quad (7)$$

where $u = \sqrt{l_{i1}^2 + l_{i2}^2 + l_{i3}^2 - l_{i1}l_{i2} - l_{i1}l_{i3} - l_{i2}l_{i3}}$.

Because the Taylor series expansion was carried out at $q_i = 0$, MSF's are numerically well posed for the complete ranges of length variables. Because of the redundancy of R_i in equation (3) (i.e., $[R_i]_{21} = [R_i]_{21}$, $[R_i]_{31} = [R_i]_{13}$, and $[R_i]_{32} = [R_i]_{23}$), modal HTM for any continuum section of similar actuator arrangement can be completely defined by nine distinct MSF's (six from R_i and three from p_i).

3.2. Choosing the Taylor series expansion order

Accuracy is an important aspect in any engineering approximation method. A prototype continuum section, to which the modal kinematics is derived, exhibits $\phi_{i:\max}$ close to 184° (when $l_{i1} = 0$ and $l_{i2} = l_{i3} = 0.06$ m). For this maximum bending, the maximum percentage error (%Err_{max}) variation for all the unique elements of modal HTM against Taylor series expansion order is shown in figure 10. In this paper, %Err_{max} less than 1% per modal HTM element

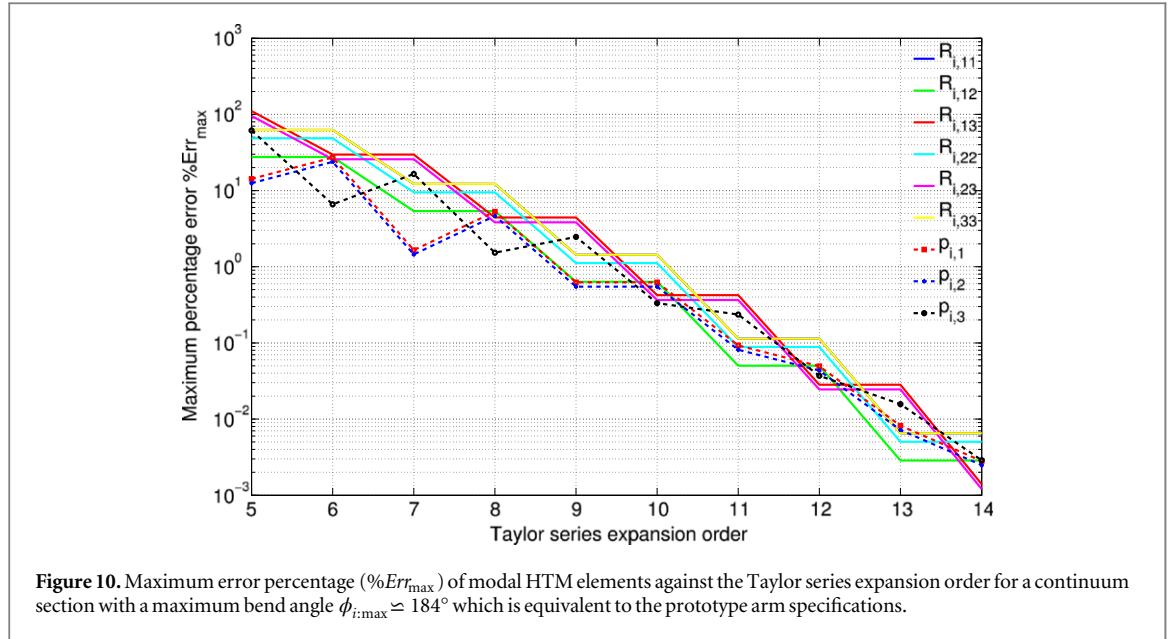


Figure 10. Maximum error percentage ($\%Err_{\max}$) of modal HTM elements against the Taylor series expansion order for a continuum section with a maximum bend angle $\phi_{i:\max} \simeq 184^\circ$ which is equivalent to the prototype arm specifications.

Table 1. Normalized maximum percentage errors ($\%Err_{\max}$) of a single continuum section modal HTM elements.

	$\%Err_{\max}$ of \mathbf{R}_i^a		$\%Err_{\max}$ of \mathbf{p}_i
0.114 ^b	0.050	0.423	0.092
0.050	0.088	0.366	0.081
0.423	0.366	0.114	0.235

^a Continuum section with $\phi_{i:\max} \simeq 184^\circ$.

^b The normalized errors are computed as follows. First, the range of any $[\mathbf{T}_i^c]_{jk}$ is computed as $\max([\mathbf{T}_i^c]_{jk}) - \min([\mathbf{T}_i^c]_{jk})$. Then the maximum error, $\max(|[\mathbf{T}_i]_{jk} - [\mathbf{T}_i^c]_{jk}|)$, is found and the normalized errors are calculated as $\%Err_{\max} = 100 \cdot \max(|[\mathbf{T}_i]_{jk} - [\mathbf{T}_i^c]_{jk}|) / [\max([\mathbf{T}_i^c]_{jk}) - \min([\mathbf{T}_i^c]_{jk})]$. Note that, limiting values are considered within singular conditions.

was considered acceptable. Therefore, based on the figure 10, to achieve the desired accuracy, an order 11 expansion for all modal HTM elements were chosen. Table 1 lists the corresponding normalized $\%Err_{\max}$ for all unique elements of modal HTM. It can be observed that the $\%Err_{\max}$ for all elements are less than 0.5%. This corresponds to a absolute and normalized (to the unactuated continuum section length, L_{i0}) maximum position errors at the arm tip 0.000 62 m and 0.0041 respectively which are more than required.

The procedure for assessing the required Taylor series expansion order can be mathematically generalized and extended for any continuum arms with differing physical characteristics as follows.

The $\%Err_{\max}$ of any modal HTM element is directly proportional to $\phi_{i:\max}$ (when $l_{i1} = l_{i:\min}$ and $l_{i2} = l_{i3} = l_{i:\max}$), and inversely proportional to the expansion order. Figure 11 shows the dependency of $\%Err_{\max}$ (among all unique modal HTM elements)

with the expansion order and $\phi_{i:\max}$. Hence, by knowing the $\phi_{i:\max} \in [0, 2\pi]$ of any i th continuum section and required accuracy, the minimum order of Taylor series expansion for any HTM element can be found. Utilizing curve fitting techniques, the resulting surface can be approximated to a forth order bivariate polynomial (degree 3 in $\phi_{i:\max}^3$ and degree 1 in expansion order) and is given by

$$\text{Expansion order} \geq \text{ceiling} \left\{ \frac{\text{Log}_{10}(\%Err_{\max}) - k_1}{k_2} \right\}, \quad (8)$$

where $k_1 = 16.14 + 1.86\phi_{i:\max} - 0.63\phi_{i:\max}^2 + 0.06\phi_{i:\max}^3$ and $k_2 = -2.94 + 0.66\phi_{i:\max} - 0.05\phi_{i:\max}^2$.

Therefore, to find the expansion for a given continuum section to meet a desired $\%Err_{\max}$, one simply has to compute $\phi_{i:\max}$ and apply in equation (8) to obtain the optimal expansion order.

3.3. Advantages of the proposed modal method

The Taylor series based approach for deriving MSF's has several advantages over other traditional modal methods. First, it provides an intuitive and straightforward choice to produce unique MSF per HTM element, based on structurally accurate kinematics. Thus it avoids modal switching and modal singularities (Chirikjian 1994). Also, both forward and inverse kinematics can be computed directly in the joint space without the need for additional singularity resolving methods such as those reported in (Jones and Walker 2007, Rolf and Steil 2012). In addition, no intermediary transformations are required to map specific shapes and thus the method avoids re-deriving MSF's for varying applications or requirements. The proposed method can be easily extended to dynamically model multisection continuum arms since the polynomial expressions can be readily integrated and efficiently evaluated.

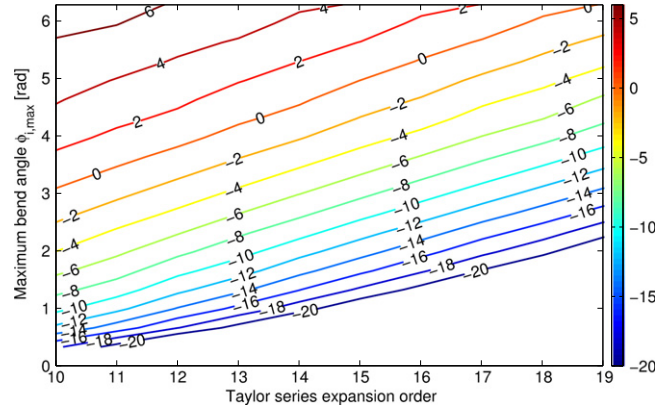


Figure 11. Maximum error percentage of (among all elements of T_i) in Log_{10} scale, (the color bar on the right) against maximum bending angle, $\phi_{i,\max}$, and Taylor series expansion order. Maximum bend angle was calculated by using equation (2) for ϕ_i .

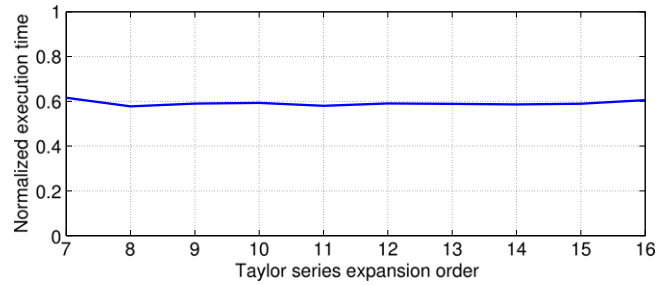


Figure 12. Computation time comparison of modal HTM order vs curve parametric HTM. The execution time is normalized to the execution time of T^c ($25.2 \mu\text{s}$). The mean execution time was calculated averaging the time for 1000 computations for random variable q_i combinations.

Computational performance versus modal HTM order are shown in figure 12 where the execution times are compared against the CP HTM. All modal HTM's demonstrate consistently less execution times around 0.6 though the number of polynomial terms increases with expansion order. This can be explained as follows. MSF's use powers of same algebraic terms to construct the terms of the Taylor series expansion. Hence it is computationally efficient with regards to trigonometric functions used in CP models. These results demonstrate the superior performance of the modal kinematics for continuum arms.

4. Modal kinematics for multisection continuum arms

Analogous to deriving HTM for multi-linked rigid robotic arms, the modal HTM for a single continuum section is extended to formulate the modal kinematics of multisection continuum arms. Considering a general case, the schematic of a continuum arm with an arbitrary N number of sections is illustrated in figure 13. The continuum sections are incrementally numbered starting from 1 for the lowermost section attached to the origin of the task coordinate frame, OXYZ or $\{O\}$, while the remaining sections are attached to one another rigidly at the connection point.

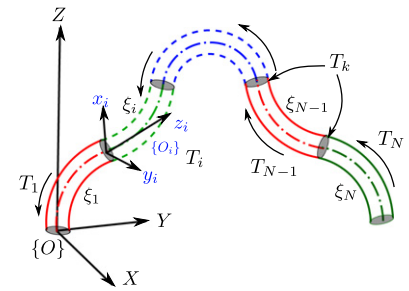


Figure 13. Schematic of a general multisection continuum arm with N continuum sections.

4.1. Forward kinematics

Using basic coordinate transformations, the modal HTM for the neutral axis of the entire arm relative to $\{O\}$ is calculated as

$${}^N_0\mathbf{T}(\mathbf{q}, \boldsymbol{\xi}) = \prod_{k=1}^N \left\{ {}^k_{k-1}\mathbf{T}(\mathbf{q}_k, \xi_k) \mathbf{T}_k^I \right\} = \begin{bmatrix} \boldsymbol{\Theta}_N(\mathbf{q}, \boldsymbol{\xi}) & \boldsymbol{\Psi}_N(\mathbf{q}, \boldsymbol{\xi}) \\ \mathbf{0}_{1 \times 3} & 1 \end{bmatrix}, \quad (9)$$

where $\boldsymbol{\Theta}_N \in SO(3)$ is the modal rotational matrix, $\boldsymbol{\Psi}_N \in \mathbb{R}^3$ is the modal translation vector, $\mathbf{q} = [q_1, q_2, \dots, q_N]^T \in \mathbb{R}^{3N}$ is the composite joint space vector that uniquely describes the configuration

Table 2. Evaluation of ξ from the base to the end section along the neutral axis.

Continuum section number	ξ_1	ξ_2	\dots	ξ_{N-1}	ξ_N
1	ξ_1	0	\dots	0	0
2	1	ξ_2	\dots	0	0
\vdots	\vdots	\vdots	\ddots	0	0
$N-1$	1	1	1	ξ_{N-1}	0
N	1	1	1	1	ξ_N

E.g.: For $\xi = 3.3$, $\xi_i = 1 \forall i \leq 3$, $\xi_i = \text{mod}(\xi, 1) = 0.3$ for $i = \text{ceiling}(\xi)$, i.e., $\xi = [1, 1, 1, 0.3, \dots, 0]^T$.

of the entire arm, $\mathbf{T}_k^J \in SE(3)$ are constant HTM's that account for position/orientation offsets at section joints, and $\xi = [\xi_1, \xi_2, \dots, \xi_N]^T \in \mathbb{R}^N$ is the vector of scalar coefficients evaluated as shown in table 2.

The idea behind the ξ notation is that the position and orientation of any i th continuum section of the arm depends on the preceding continuum sections up to $(i-1)$ th but is independent of the successive sections. This dependency is accounted for by making $\xi_k = 1$, $\forall k < i$ and $\xi_k = 0$, $\forall k > i$ while ξ_i denotes the points along the i th continuum section. Hence $\xi = [0, N]$ collectively indicate any point along the arm. For the ease of notation for subsequent derivations it is assumed from this point onward that respective joint HTM's, \mathbf{T}_k^J , are integrated in the overall continuum section modal HTM's ($\mathbf{T}_i \leftarrow \mathbf{T}_i^J \mathbf{T}_i^J$). This can be done without difficulty because the resulting modal HTM's will consist of linear combinations of previously derived MSF's.

The θ_i and ψ_i can be implemented recursively with the iterative use of modal \mathbf{R}_i and \mathbf{p}_i . The rotation matrix Θ_i of the i th section is given by

$$\Theta_i = \mathbf{R}_1 \mathbf{R}_2 \mathbf{R}_3 \dots \mathbf{R}_{i-1} \mathbf{R}_i, \quad (10)$$

where $\mathbf{R}_i = R(L_{i0}, r_i, \mathbf{q}_i, \xi_i)$ is the functional implementation of the rotation matrix and $R(0, 0, \mathbf{0}, 0) \equiv \mathbf{I}$.

The equation (10) can be simplified using the definition $\Theta_{i-1} = \mathbf{R}_1 \mathbf{R}_2 \dots \mathbf{R}_{i-1}$ as follows

$$\Theta_i = (\mathbf{R}_1 \mathbf{R}_2 \mathbf{R}_3 \dots \mathbf{R}_{i-1}) \mathbf{R}_i = \Theta_{i-1} \mathbf{R}_i. \quad (11)$$

Similar to the rotation matrix, the translation vector of the i th section is given by

$$\psi_i = \mathbf{p}_1 + \mathbf{R}_1 \mathbf{p}_2 + \dots + \mathbf{R}_1 \mathbf{R}_2 \dots \mathbf{R}_{i-1} \mathbf{p}_i, \quad (12)$$

where $\mathbf{p}_i = p(L_{i0}, r_i, \mathbf{q}_i, \xi_i)$ is the functional implementation of the position vector with $p(0, 0, \mathbf{0}, 0) \equiv \mathbf{0}$.

Employing the results of equation (11) and the definition of ψ_{i-1} , equation (12) is simplified as

$$\begin{aligned} \psi_i &= (\mathbf{p}_1 + \dots + \mathbf{R}_1 \dots \mathbf{R}_{i-2} \mathbf{p}_{i-1}) + (\mathbf{R}_1 \dots \mathbf{R}_{i-1}) \mathbf{p}_i \\ &= \psi_{i-1} + \Theta_{i-1} \mathbf{p}_i. \end{aligned} \quad (13)$$

Therefore, the forward kinematics for continuum arms with any number of sections is completely described by nine MSF's. Note that, one may exclude

Table 3. Normalized maximum percentage errors (%Err_{max}) of modal HTM elements at the tip of the prototype continuum arm.

	%Err _{max} of Θ_3^a		%Err _{max} of Ψ_3
0.88 ^b	0.81	1.02	0.28
0.76	0.76	1.07	0.31
0.82	1.06	0.43	0.31

^a For each continuum section, $\phi_{i:\max} \simeq 184^\circ$.

^b The normalized %Err_{max} were computed similar to the procedure given in table 1.

r_i and L_{i0} as variables of the MSF implementations if the multisection continuum arm is composed of mechanically identical continuum sections similar to the prototype arm described in this paper.

4.2. Error accumulation

When multiple continuum sections are stacked together, the errors of each unit get accumulated when moving toward the arm tip. Thus the initial approximation, which was considered suitable for a single section determines the overall accuracy of the kinematic model and may not be adequate for the multisection case. In this paper, an absolute and normalized (to the unactuated length, $3L_0$) position error of 0.005 m and 1% at the three-section arm end was considered acceptable. Therefore the original 11th order Taylor series expansion which resulted 0.0043 m maximum position error is adequate. The normalized element errors of the resulting modal HTM are listed in table 3.

4.3. Orientation kinematics

Orientation kinematics for arm points, generally when $\xi \geq 3$, can be defined for multisection continuum arms. Let the Euler angle vector about ZXX axes rotations be $\boldsymbol{\varphi} = [\alpha, \beta, \gamma]^T$. These angles can be related to Θ_N of equation (9) as

$$\mathbf{R}_Z(\alpha) \mathbf{R}_X(\beta) \mathbf{R}_Z(\gamma) = \Theta_N(\mathbf{q}, \xi). \quad (14)$$

The inverse relationship of these orientation parameters can be used to compute the orientation at ξ of the continuum arm (Siciliano and Khatib 2008). The angles $\{\alpha, \beta, \gamma\}$ can be calculated from the elements of Θ_N given by equation (14) as

$$\begin{aligned} \alpha &= \text{atan2}\left(\left[\Theta_N\right]_{13}, -\left[\Theta_N\right]_{23}\right) \\ \beta &= \text{atan2}\left(-\left[\Theta_N\right]_{23} \cos \alpha + \left[\Theta_N\right]_{13} \sin \alpha, \left[\Theta_N\right]_{33}\right) \\ \gamma &= \text{atan2}\left(\left[\Theta_N\right]_{31}, \left[\Theta_N\right]_{32}\right). \end{aligned}$$

4.4. Velocity kinematics and the modal Jacobian

Because of the redundancy of multisection continuum arms, inverse kinematics rely on iterative methods which are based on the Jacobian matrix to relate task-space and joint space velocities (Selig 1992). Utilizing the modal HTM for a general arm, the modal Jacobian

matrix can be defined for the multisection continuum robot as follows.

The linear velocity along the neutral axis with reference to $\{O\}$, denoted by $v \in \mathbb{R}^3$, is given by

$$v(q, \dot{q}, \xi) = J^v(q, \xi) \dot{q}, \quad (15)$$

where $J^v = \Psi_{N,q} \in \mathbb{R}^{3 \times 3N}$ is the linear velocity Jacobian, the subscript followed by a comma, i.e., $[\]_{,h}$, denotes the partial derivative operator $\left(\frac{\partial}{\partial h}\right)$ with respect to the given vector or variable. In case of a vector (i.e., $h = [h_1, h_2, \dots, h_N]$), the result is a row vector of partial derivatives with respect to the elements of vector h as $[\]_{,h} \equiv [\frac{\partial}{\partial h_1}, \frac{\partial}{\partial h_2}, \dots, \frac{\partial}{\partial h_N}]$.

Similarly, the angular velocity with respect to $\{O\}$, $\omega \in \mathbb{R}^3$ can be derived from the skew symmetric angular velocity matrix (Murray et al 1994), $\Omega = \dot{\Theta}_N \Theta_N^T \in SO(3)$ and given by

$$\omega(q, \dot{q}, \xi) = \left\{ \dot{\Theta}_N(q, \dot{q}, \xi) \Theta_N^T(q, \xi) \right\}^\vee = \Omega(q, \dot{q}, \xi)^\vee = J^\omega(q, \xi) \dot{q}, \quad (16)$$

$$\text{where } \omega = [\omega_x, \omega_y, \omega_z]^T, \Omega = \begin{bmatrix} 0 & -\omega_z & \omega_y \\ \omega_z & 0 & -\omega_x \\ -\omega_y & \omega_x & 0 \end{bmatrix},$$

$J^\omega = (\Theta_{N,q} \Theta_N^T)^\vee \in \mathbb{R}^{3 \times 3N}$, and the operator \vee is defined as $\Omega^\vee = \omega$ to construct ω from Ω .

By combining the linear and angular velocities, the spatial velocity of any point with respect to $\{O\}$, $V^s \in \mathbb{R}^{6 \times 3N}$ is given by

$$V(q, \dot{q}, \xi) = \begin{bmatrix} v \\ \omega \end{bmatrix} = \begin{bmatrix} J^v \\ J^\omega \end{bmatrix} \dot{q} = J(q, \xi) \dot{q},$$

where $J \in \mathbb{R}^{6 \times 3N}$ is the composite modal Jacobian matrix.

Similar to modal HTM, J is also numerically well posed under singular conditions and provides reliable results within the complete range of joint space variables.

4.5. Efficient numerical implementation

Since continuum sections are decoupled in a multisection arm, taking the partial differentiations of joint variables only affect the matrices of the relevant continuum section i.e., $R_{i,q_j} = 0 \ \forall q_j \notin q_i$. Also, all the continuum sections share a similar physical structure, the partial derivatives only have to be derived for generic modal R_i and p_i . Therefore, the calculation of the modal Jacobian matrix can be carried out recursively by reusing the functions for modal matrices, R_i and p_i and their partial derivatives. This is accomplished by decomposing equations (15) and (16) into a series of rotational matrices, R_i , position vectors, p_i and their partial derivatives. The resulting recursive implementation of linear and angular modal Jacobian matrices are given below.

4.5.1. Angular velocity Jacobian

From the equation (16), the angular velocity modal Jacobian of the i th section, J_i^ω is given by

$$J_i^\omega = (\Theta_{i,q^i} \Theta_i^T)^\vee,$$

where $q^i = [q_1, q_2, \dots, q_i]^T \in \mathbb{R}^{3i}$.

Define the j th column of J_i^ω as

$$(J_i^\omega)_j = (\Theta_{i,q_j} \Theta_i^T)^\vee, \quad (17)$$

where $(\)_j$ denotes the j th column of the corresponding matrix, $q_j \in q^i$ ($j \leq 3i$) is any joint space variable in $q^{i-1} = [q_1, q_2, \dots, q_{i-1}]^T \in \mathbb{R}^{3(i-1)}$, and the operator \wedge is the inverse operator of \vee which produces the skew symmetric matrix from a column vector, i.e., $\omega^\wedge = \Omega$.

Depending on whether q_j belongs to q^{i-1} or q_i , the result can be simplified in two separate cases. Note that $q^i = [q^{i-1} q_i] \in \mathbb{R}^{3i}$. When $q_j \in q^{i-1}$, substituting equation (11) into equation (17) and simplification results in

$$\begin{aligned} (J_i^\omega)_j &= \left\{ \Theta_{i-1,q_j} (R_i R_i^T) \Theta_{i-1}^T \right\}^\vee = (\Theta_{i-1,q_j} \Theta_{i-1}^T)^\vee \\ &= (J_{i-1}^\omega)_j, \end{aligned}$$

where $R_i R_i^T = I$.

Similarly, when $q_j \in q_i$, equation (17) becomes

$$(J_i^\omega)_j = (\Theta_{i-1} R_{i,q_j} R_i^T \Theta_{i-1}^T)^\vee.$$

By combining these results, any column of an i section Jacobian can be expressed in recursive form as

$$(J_i^\omega)_j = \begin{cases} (J_{i-1}^\omega)_j & ; q_j \in q^{i-1}, \\ (\Theta_{i-1} R_{i,q_j} R_i^T \Theta_{i-1}^T)^\vee & ; q_j \in q_i. \end{cases} \quad (18)$$

4.5.2. Linear velocity Jacobian

Likewise from the equation (15), consider the general case linear velocity Jacobian of the i th section, J_i^v , of a multisection continuum arm

$$J_i^v = \Psi_{i,q^i}.$$

The j th column vector of J_i^v is defined as $(J_i^v)_j$ and given by

$$(J_i^v)_j = \Psi_{i,q_j}, \quad (19)$$

where $q_j \in q^i$.

When $q_j \in q^{i-1}$ substituting equation (13) into (19) gives

$$(J_i^v)_j = \Psi_{i-1,q_j} + \Theta_{i-1,q_j} p_i. \quad (20)$$

Adding the term $\Theta_{i-1}^T \Theta_{i-1} = I$ without modifying the result and simplifying equation (20) yields

$$\begin{aligned}
(\mathbf{J}_i^v)_j &= \Psi_{i-1,q_j} + \Theta_{i-1,q_j} (\Theta_{i-1}^T \Theta_{i-1}) \mathbf{p}_i \\
&= \Psi_{i-1,q_j} + \left(\Theta_{i-1,q_j} \Theta_{i-1}^T \right) \Theta_{i-1} \mathbf{p}_i \\
&= (\mathbf{J}_{i-1}^v)_j + (\mathbf{J}_{i-1}^o)_j \Theta_{i-1} \mathbf{p}_i.
\end{aligned}$$

When $q_j \in \mathbf{q}_i$, equation (19) results in

$$(\mathbf{J}_i^v)_j = \Theta_{i-1} \mathbf{p}_{i,q_j}.$$

Combining these results yields

$$(\mathbf{J}_i^v)_j = \begin{cases} (\mathbf{J}_{i-1}^v)_j + (\mathbf{J}_{i-1}^o)_j \Theta_{i-1} \mathbf{p}_i & ; q_j \in \mathbf{q}^{i-1}, \\ \Theta_{i-1} \mathbf{p}_{i,q_j} & ; q_j \in \mathbf{q}_i. \end{cases} \quad (21)$$

The results given by equations (18) and (21) complete the recursive implementation of angular and linear velocity Jacobians respectively.

The above generalized recursive relationship has utilized 36 MSF's (nine originally derived for the modal HTM, given by equation (6), and partial derivatives with respect to l_{i1} , l_{i2} , l_{i3} that can readily be derived through symbolic computer algebra systems). Note that, for continuum sections having different $\phi_{i:\max}$, one may use different order Taylor series expansions based on the derived error shown in figure 10. In order to avoid defining many MSF's and fully benefit from the recursive implementation given here, MSF's are derived to the continuum section having largest maximum bending i.e., $\phi_{\max} = \max(\phi_{i:\max} \forall i)$ therefore, the accuracy for the other continuum sections will not be an issue.

4.6. Complete inverse kinematics

Obtaining closed form inverse kinematics for the full task-space position and/or orientation for multisection continuum arms is computationally infeasible. Therefore to solve inverse kinematic problems, iterative procedures based on the multivariate Newton–Raphson approach are utilized (Buss 2004). The pseudo inverse of the modal Jacobian matrix, $\mathbf{J}^\dagger = \mathbf{J}^T (\mathbf{J}\mathbf{J}^T)^{-1}$, is implemented into the inverse kinematic algorithm due to its simplicity and efficiency. As a result of the numerical stability observed in the modal kinematics, higher solver gains are permitted in iterative calculations. Hence the algorithm rapidly converges to solutions making the proposed modal approach suitable for computing inverse kinematic solutions on board (in the order of milliseconds). Because inverse kinematics are solved in joint space this approach will incorporate joint variables within their mechanical ranges to ensure realizable solutions. Other nonlinear optimization techniques for constrained nonlinear multivariate systems can also be utilized as required (e.g. 'fmincon' of MATLAB®). As with any redundant system, these methods yield one solution out of many for a given problem and

additional constraints can be imposed for more specific solutions (Godage et al 2012a).

5. Simulation results

In this section, the mechanical details of the three-section prototype continuum arm is presented. Then static pose of the actual arm is compared against the modal kinematic model of the arm followed by the forward and inverse kinematic simulation results.

The physical parameter values that are employed in the simulations were taken from the prototype arm shown in figure 2(a). Each continuum section consists of three mechanically identical extending PMA's (shown in figure 14(a)) with $L_{i0} = 0.15$ m, $l_{i:\min} = 0$ m, and $l_{i:\max} = 0.06$ m. Silicone rubber tubes of inner diameter 7.5 mm and outer diameter 9.5 mm were used as the PMA bladders. Plastic tube union connectors (inner diameter = 4 mm) were utilized to mount the Silicone tubes at each end because of the low cost and ease of use. The pressure-supplying plastic tubes are directly pluggable to these connectors while the other end is closed with a plastic blanking plug. The Polyester braided sheath (min. inner diameter 7 mm, max. outer diameter 17 mm) is then inserted and tightened with high strength Nylon cable ties which are light weight alternatives to steel worm gear hose clamps within the operation pressure range (0–6 bars). Rigid plastic mount frames of $r_i = 0.0125$ m and 2.54 mm thickness, shown in figure 14(b), are used to mount the PMA's and also to connect the adjacent continuum sections with a $\frac{\pi}{3}$ rad angle offset about the Z' axis of the arm tip coordinate frame (see figure 5). This offset facilitates mounting PMA's without crowding and enables routing pressure supply tubes within. Actuators are constrained to operate parallel to the neutral axis at designed clearance ($\frac{\pi}{3}$ rad apart at r_i) from each other with the help of rigid plastic constrainers of thickness 2.54 mm shown in figure 14(c). The respective modal HTM of the prototype is given by

$${}^0\mathbf{T}(\mathbf{q}, \boldsymbol{\xi}) = \prod_{k=1}^3 \left\{ \mathbf{T}_k(\mathbf{q}_k, \boldsymbol{\xi}_k) \mathbf{T}_k^I \right\}, \quad (22)$$

where $\mathbf{T}_k^I = \mathbf{R}_z\left(\frac{\pi}{3}\right)$ accounts for $\frac{\pi}{3}$ rad offsets between adjacent sections.

For the position inverse kinematics problems an iterative Newton–Raphson scheme was used with termination error 0.01 m. In the complete (position and orientation) inverse kinematic problems, the nonlinear optimization algorithm 'fmincon' from MATLAB® was used. In subsequent figures, reference coordinates and arm tip coordinates are drawn for easy comparison of results.

Figure 15(a) shows the modal kinematic results compared against a static experimental pose. The arm sections were actuated to bend at different angles on a plane (for the ease of comparison) while the distal

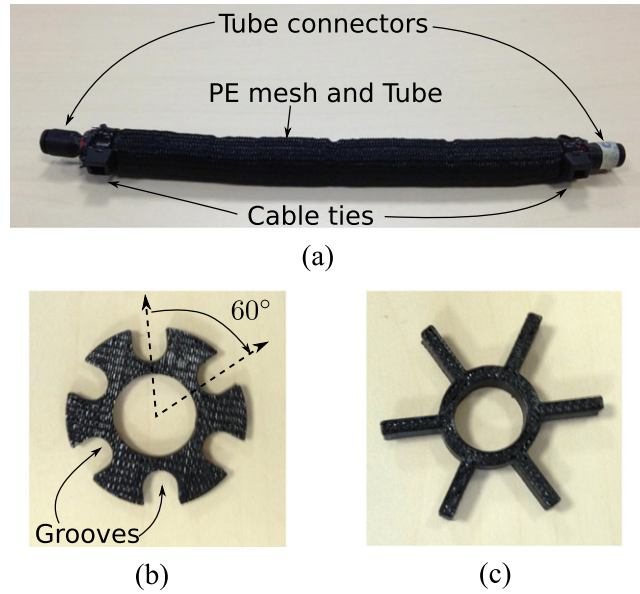


Figure 14. (a) One of the PMA's utilized in each continuum section with labeled components. (b) 3D printed rigid plastic mount frames of continuum sections where the grooves are designed to fit the tube connector dimensions. The adjacent continuum sections are affixed at a $\frac{\pi}{6}$ orientation offset as shown. (c) 3D printed plastic constrainers that are used to preserve and maintain a constant and parallel separation between PMA's.

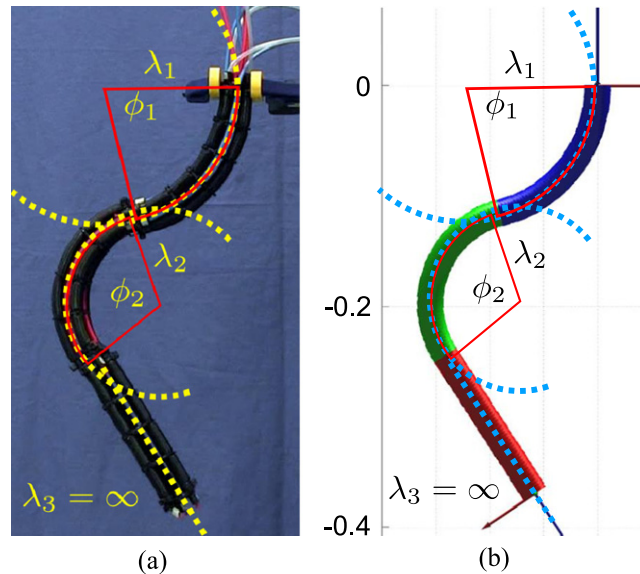


Figure 15. (a) Modal kinematic result comparison against the prototype multisection continuum arm by overlaying the curvature radii of different sections: $\{\lambda_1 = 84.22 \text{ mm}, \phi_1 = 77.1^\circ\}$, $\{\lambda_2 = 55.51 \text{ mm}, \phi_2 = 109.8^\circ\}$, and $\{\lambda_3 = \infty, \phi_3 = 0\}$ where the values are computed according to equation (2) for respective joint space variables $q_1 = [0.025, 0, 0]^T$, $q_2 = [0, 0.036, 0]^T$, and $q_3 = [0, 0, 0]^T$. (b) Direct kinematic result for the input joint space variables employed to generate figure 15(a).

section remains unactuated (therefore straight). The corresponding length changes were then computed from the static pressure and length relationships of each PMA and then applied to the proposed arm kinematic model given by equation (22). As seen in the figure, the computed and illustrated curve parameters agree very well with the experimental results. Figure 15(b) shows the forward kinematic result utilizing the modal kinematic model with the same joint

space variable values. The results comply very well with the experimental results. Note that the model accurately accounts for the singular straight arm pose without difficulty.

5.1. Performance comparison

Herein, the proposed model's (designated by MSF) computational efficiency and reliability is compared

Table 4. Computational performance comparison against MSF versus CP kinematics.

	CP	MSF
Stable	No	Yes
FK1: Straight arm motions	Fail(3.16 ^a)	2.07
FK2: Bending motions	3.14	2.08
IK1: Spiral path tracking	18.45 (55%)	18.00 (98%)
IK2: Orientation path tracking	17.82 (98%)	17.77 (98%)

^a The computational times are normalized to the execution time of $T^c = 25.2 \mu s$.

against the CP model. Table 4 shows the normalized time performance for two forward kinematic (denoted FK1 and FK2) and two inverse kinematic simulations (denoted IK1 and IK2).

The first simulation (FK1) is a forward kinematic elongation and contraction (shown in figure 16(a)) for which the MSF yields correct results whereas CP was undefined due to the singularity problem. Then for bending results (FK2; shown in figure 16(b)), the computation time was measured for each step and the mean value obtained. Both models yielded correct results but the MSF were considerably faster than that of CP implementation.

Comparison between the iteratively solved inverse position tracking (shown in figure 17(b)) is listed under IK1. Because there is a singular pose at the end, the success rate of correct tracking for the CP model drastically reduced ($\sim 55\%$). Due to the flexible 0.01 m termination error sometimes the CP model was able to converge to a solution while avoiding singularities of all three sections. Since the solution was within the singularity neighborhoods the iterative scheme becomes unstable due to large errors discussed in section 2.3, thus resulting in low success rate. Thence the CP model is not reliable whereas the MSF model produced reliable results efficiently throughout. Likewise, inverse position and orientation tracking results (corresponding results are shown in figure 19(a)) are compared under IK2. For both inverse kinematic cases, the CP and MSF methods recorded comparable times but the MSF method showed higher reliability.

5.2. Forward kinematics

The straight arm movements in figure 16(a) are achieved by maintaining the singular pose actuator relationship $l_{i1} = l_{i2} = l_{i3}$ by gradually increasing all actuators l_{ij} to l_{\max} and back to l_{\min} . This exemplifies the advantage of the joint space implementation to limit the actuation range to obtain physically realizable poses. Results for bending, shown in figure 16(b), are obtained by increasing the length parameter values in only the third actuator (l_{i3}) for each section from the unactuated original state at a ratio of $l_{i3} : l_{i23} : l_{i33} = 3 : 4 : 5$ until $l_{i33} = l_{\max}$. This causes the entire arm to bend as shown. Straight arm poses are undefined for the CP model and would require

additional singularity resolving schemes but the MSF model handles both straight arm and bending poses accurately and efficiently without any issues.

5.3. Inverse position kinematics

An important feature of the new model is its efficient and complete inverse kinematic solutions. Figure 17(a) shows the simulation results for tracking an arc-shaped spatial trajectory in the XZ plane defined by $p_{\text{track}} = [0.35 \sin(\pi t) \cos(5t), 0.35 \sin(\pi t) \sin(5t), 0.83t - 0.2]^T \in \mathbb{R}^3$. Simulation results in figure 17(b) depict the arm tracking a spiral shape trajectory mathematically represented by $p_{\text{track}} = [0.25 \sin(\pi t), 0, -0.2 + 0.83t]^T$. To accomplish the tracking, a series of tracking coordinates along the trajectory were iteratively fed to the inverse kinematic solver. The termination point of the trajectory is a pure extending pose with $l_{ij} = l_{\max} : \forall i, j$, where both the position vectors and Jacobians in previous CP models would be singular. But with the MSF model the inverse kinematic solver efficiently converges to solutions without numerical instabilities.

Figure 18 shows solution convergence times for 100 specified points along the trajectory shown in figure 17(b). The computation was executed in MATLAB[®] environment on a computer having a 2.3 GHz processor and 8GB RAM. It is observed that the algorithm rapidly converges to solutions (average time is ~ 1 ms). The peak at the beginning corresponds to the initial solution time for the random starting point. This can be implemented in on-board controllers to perform real-time model based inverse kinematic computations for kinematic control of multi-segment continuum arms (Walker 2007).

5.4. Inverse kinematics for position with orientation

Inverse kinematic tracking results with different arm tip orientations are shown in figures 19(a), (b), and (c) for a spatial trajectory $p_{\text{track}} = [0.3 - 0.2t, 0.1, 0.2 + 0.25t]^T$. The arm tip was tracked to follow three different fixed orientations and iteratively solved using MATLAB[®] 'fmincon' constrained optimization routine. The results show that the arm tip is able to track the given line with varying orientations. Similarly, figure 19(d) demonstrates varying arm tip orientation, $\varphi(t) = [\frac{\pi}{2}(2 - t), 0, 0]^T$, at a fixed arm tip position, $\mathcal{P}_3 = [0, -0.2, 0.3]^T$. The simulations exemplify the proposed model's capability to correctly represent both forward and inverse kinematics without numerical instabilities. This kinematic decoupling feature has not been previously demonstrated and allows for the arm tip position and orientation to be controlled independently. This feature is exploited to produce useful application scenarios in the next section.

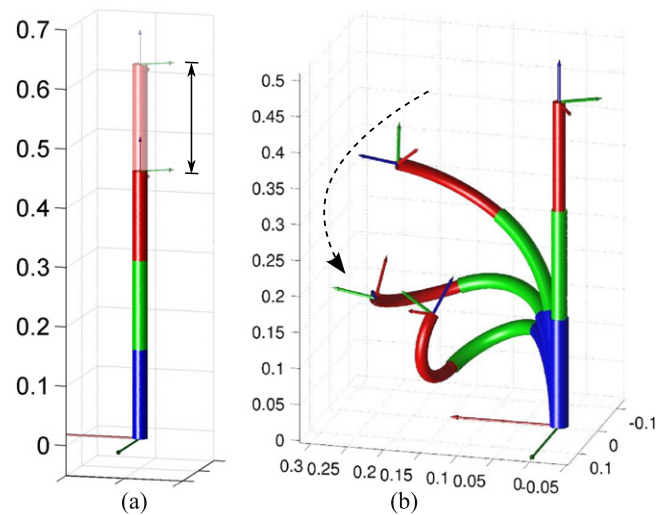


Figure 16. Forward kinematic results (a) pure extension and contraction from original length to maximum extension along Z axis and back (b) bending each continuum section at different rates.

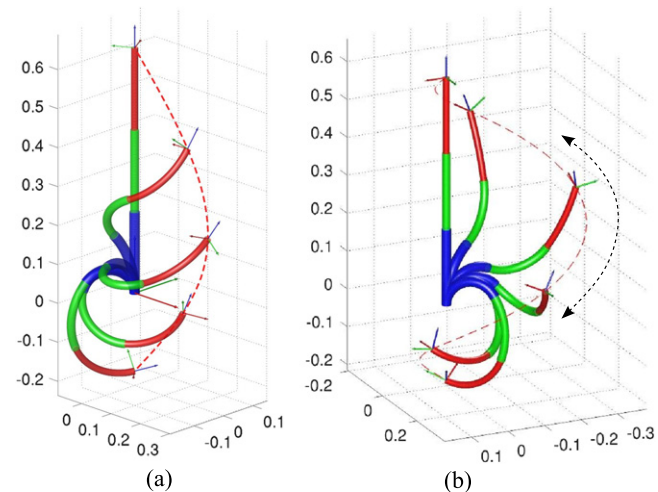


Figure 17. Inverse position kinematics: (a) the arm tip tracking a arc shaped trajectory, and (b) the arm tip tracking a spiral trajectory.

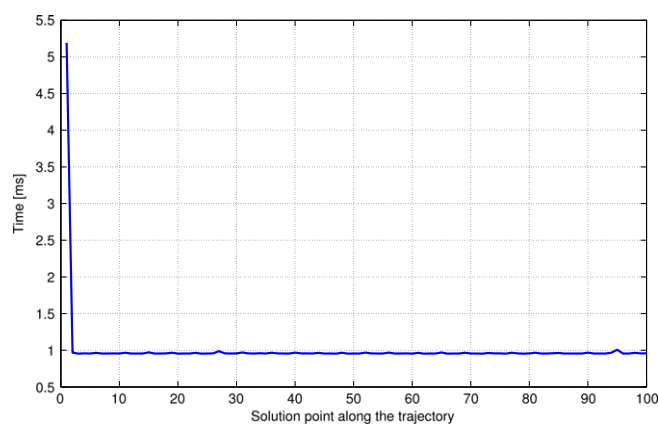
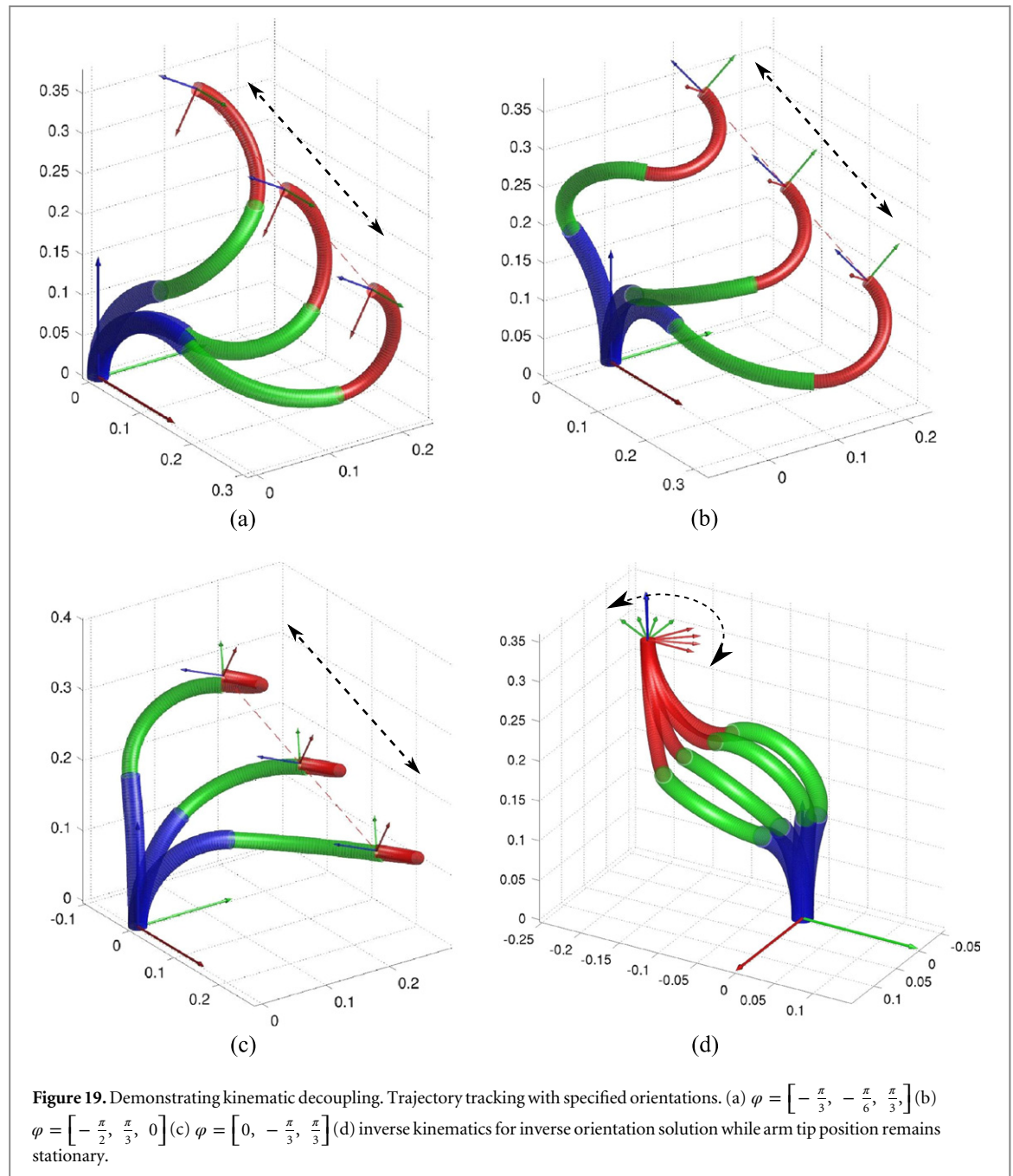


Figure 18. Computing efficiency for inverse kinematic solution computations for 3 constraint trajectory tracking problem from figure 17(b).



5.5. Application examples

Object inspection tasks involve inverse kinematic solutions for variable position and orientation constraints while adhering to actuator limits. Robotized minimally invasive surgery is one such example where positioning and orientation are both critical (Simaan *et al* 2004). Inspection tasks on irregular shaped objects is another application. Figure 20(a) shows a multisection continuum arm inspecting a spherical object by aiming a hypothetical camera mounted on the arm tip while maintaining constant distance from the object surface. The object shape was chosen for its convenient mathematical properties, but other shapes can be easily accommodated.

Whole arm manipulation is another unique application that can be naturally observed in elephant trunks and octopus arms (Salisbury 1988). To demonstrate this feature, an additional fourth continuum section is fitted to the three-section continuum arm for grasping purposes while the remaining sections achieve the desired position and orientation. figure 20(b) illustrates the handling of a spherical object in a fixed orientation while tracking a spatial trajectory. This leads to object maneuvering applications that require particular orientation such as handling a water bucket without spilling. With more sections dedicated to grasping the size and complexity of the handled object can be increased.

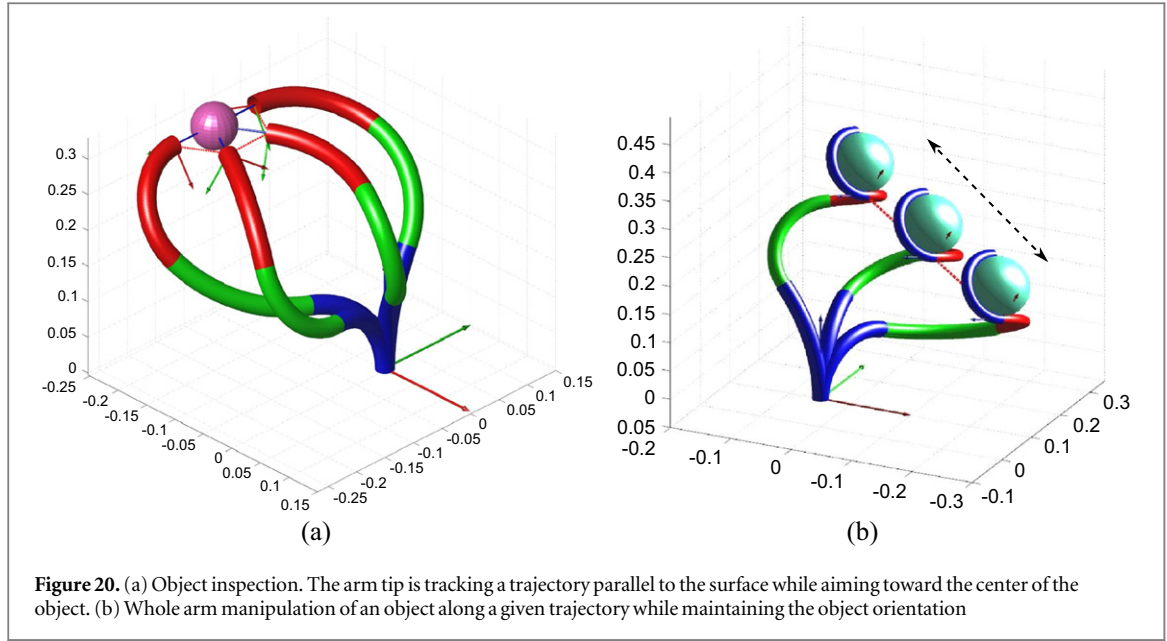


Figure 20. (a) Object inspection. The arm tip is tracking a trajectory parallel to the surface while aiming toward the center of the object. (b) Whole arm manipulation of an object along a given trajectory while maintaining the object orientation

6. Conclusions

The new modal approach presented in this paper facilitates intuitive derivation of MSF's, circumvents the kinematic singularities existing in previously proposed approaches, and introduces inverse kinematics for position and orientation. Also, MSF's derived for one section can be implemented functionally and used for other continuum sections. The numerical stability of the model results in efficient iterative numerical solutions for inverse kinematic problems. In addition, kinematic problems are solved directly in the joint space without using intermediary transformations or curve parameters, thus providing enhanced insight into the practical mechanics of continuum robot arms. The proposed model is also easily extended to any geometrically constrained variable length multisection continuum arm.

Acknowledgments

This work was in part supported by the European Commission in the ICT-FET OCTOPUS Integrating Project, under contract n. 231 608-999596447.

Authors would like to thank I D Walker at Clemson University for his helpful comments and feedback.

Appendix A. CP kinematics

A.1. Deriving curve parameters in joint space variables

Let the origin of the task-space coordinate frame $\{O_i\}$ coincide with the center of the base plate where $\overrightarrow{O_i A_1}$ marks the X_i axis. The actuator attaching points

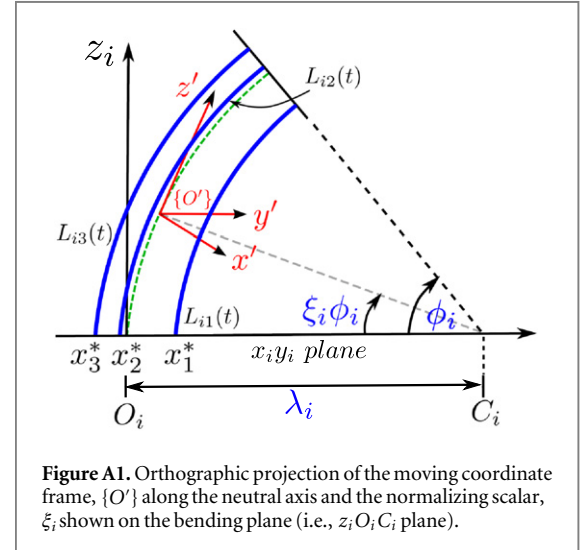


Figure A1. Orthographic projection of the moving coordinate frame, $\{O'\}$ along the neutral axis and the normalizing scalar, ξ_i , shown on the bending plane (i.e., $z_i O_i C_i$ plane).

makes an equilateral triangle of sides $r_i \sqrt{3}$ at each end of the continuum section. The coordinates of actuator attaching points are $A_1 = [r_i, 0, 0]^T$, $A_2 = \frac{r_i}{2}[-1, \sqrt{3}, 0]^T$, and $A_3 = -\frac{r_i}{2}[1, \sqrt{3}, 0]^T$. The instantaneous center of the bent arm's circular arc shape is C_i . Figure A1 shows the actuator base points, A_1, A_2 and A_3 , projected onto $\overrightarrow{O_i C_i}$ which intersect at x_1^*, x_2^* , and x_3^* . The respective distances between O_i and intersection points are

$$\begin{aligned} O_i x_1^* &= r_i \cos \theta_i \\ O_i x_2^* &= r_i \cos \left(\frac{2\pi}{3} - \theta_i \right) \\ O_i x_3^* &= r_i \cos \left(\frac{4\pi}{3} - \theta_i \right). \end{aligned} \quad (\text{A.1})$$

The actuator lengths form radii of three concentric circular arcs of varying curvature radius at

$O_i C_i$ (see figure A1). Employing arc geometrical relationship arc length = curvature radius \times subtended angle, the actuator lengths are related to curve parameters as

$$\begin{aligned} L_{i0} + l_{i1} &= (\lambda_i - O_i x_1^*) \phi_i \\ &= \left\{ \lambda_i - r_i \cos(\theta_i) \right\} \phi_i \end{aligned} \quad (\text{A.2})$$

$$\begin{aligned} L_{i0} + l_{i1} &= (\lambda_i - O_i x_2^*) \phi_i \\ &= \left(\lambda_i + \frac{1}{2} r_i \cos \theta_i - \frac{\sqrt{3}}{2} r_i \sin \theta_i \right) \phi_i \end{aligned} \quad (\text{A.3})$$

$$\begin{aligned} L_{i0} + l_{i1} &= (\lambda_i - O_i x_3^*) \phi_i \\ &= \left(\lambda_i + \frac{1}{2} r_i \cos \theta_i + \frac{\sqrt{3}}{2} r_i \sin \theta_i \right) \phi_i. \end{aligned} \quad (\text{A.4})$$

These relationships are now manipulated to derive curve parameters in joint space variables. Summing up equations (A.2), (A.3) and (A.4) yields

$$\begin{aligned} 3\lambda_i \phi_i &= 3L_{i0} + l_{i1} + l_{i2} + l_{i3} \\ \phi_i &= \frac{1}{3\lambda_i} (3L_{i0} + l_{i1} + l_{i2} + l_{i3}). \end{aligned} \quad (\text{A.5})$$

Subtracting equation (A.3) from equation (A.4) and rearranging the terms produces

$$\begin{aligned} l_{i3} - l_{i2} &= (\sqrt{3} r_i \sin \theta_i) \phi_i \\ \sin \theta_i &= \frac{l_{i3} - l_{i2}}{\sqrt{3} r_i \phi_i}. \end{aligned} \quad (\text{A.6})$$

Similarly, rearranging equation (A.2) gives

$$\cos \theta_i = \frac{\lambda_i \phi_i - (L_{i0} + l_{i1})}{r_i \phi_i}. \quad (\text{A.7})$$

Applying equations (A.6) and (A.7) to the trigonometric identity $\sin^2 \theta_i + \cos^2 \theta_i = 1$, to remove θ_i from the relationship, results in

$$\left(\frac{l_{i3} - l_{i2}}{\sqrt{3} r_i \phi_i} \right)^2 + \left(\frac{\lambda_i \phi_i - (L_{i0} + l_{i1})}{r_i \phi_i} \right)^2 = 1. \quad (\text{A.8})$$

Substituting ϕ_i from equation (A.5) in (A.8) and solving for $\lambda_i \in \mathbb{R}^+$ gives

$$\lambda_i(q_i) = \frac{(3L_{i0} + l_{i1} + l_{i2} + l_{i3}) r_i}{2\sqrt{l_{i1}^2 + l_{i2}^2 + l_{i3}^2 - l_{i1}l_{i2} - l_{i1}l_{i3} - l_{i2}l_{i3}}}. \quad (\text{A.9})$$

The result given by equation (A.9) is then substituted in equation (A.5) to solve ϕ_i as

$$\phi_i(q_i) = \frac{2\sqrt{l_{i1}^2 + l_{i2}^2 + l_{i3}^2 - l_{i1}l_{i2} - l_{i1}l_{i3} - l_{i2}l_{i3}}}{3r_i}. \quad (\text{A.10})$$

Dividing equation (A.6) by (A.7) yields θ_i as

$$\theta_i(q_i) = \tan^{-1} \left(\frac{\sqrt{3} (l_{i3} - l_{i2})}{l_{i2} + l_{i3} - 2l_{i1}} \right). \quad (\text{A.11})$$

The curve parameters λ_i , ϕ_i , and θ_i are now expressed in joint space variables. This approach can simply be extended to discrete/segmented tendon based continuum arms such as Gravagne and Walker (2000) to obtain the curve parameters as shown in figure A2 (a). Similar to a continuum arm case, for a continuum section with n segments the respective length relationships are given in equation (A.12)

$$\begin{aligned} L_{i0} + l_{i1} &= 2n \left\{ \lambda_i - r_i \cos \theta_i \right\} \sin \left(\frac{\phi_i}{2n} \right) \\ L_{i0} + l_{i2} &= 2n \left\{ \lambda_i - r_i \cos \left(\frac{2\pi}{3} - \theta_i \right) \right\} \sin \left(\frac{\phi_i}{2n} \right) \\ L_{i0} + l_{i3} &= 2n \left\{ \lambda_i - r_i \cos \left(\frac{4\pi}{3} - \theta_i \right) \right\} \sin \left(\frac{\phi_i}{2n} \right). \end{aligned} \quad (\text{A.12})$$

By solving for $\{\lambda_i, \phi_i, \theta_i\}$ by following a similar approach, identical orientation parameters are derived except for ϕ_i which is given as

$$\phi_i = 2n \sin^{-1} \left(\frac{u}{3nr_i} \right), \quad (\text{A.13})$$

where $u = \sqrt{l_{i1}^2 + l_{i2}^2 + l_{i3}^2 - l_{i1}l_{i2} - l_{i1}l_{i3} - l_{i2}l_{i3}}$.

A.2. Deriving the HTM for a single continuum section

Consider the moving coordinate system $\{O'\}$ shown in figures 5 and A1 along the neutral axis of the arm. Utilizing the spatial curve parameters derived in section 2.2, $\{\lambda_i, \phi_i, \theta_i\}$, the HTM for the moving frame, $\mathbf{T}_i^c \in SE(3)$, can be derived by applying the following stepwise transformations (graphically illustrated in figure A2(b) in order) starting at the base where $\{O\}$ and $\{O'\}$ coincides. First, rotate $\{O'\}$ θ_i clockwise about the z' to align the $\{O'\}$ to the bending plane. Translate λ_i amount along x' to C_i and then rotate $\xi_i \phi_i$ about the y' axis. Translate $-\lambda_i$ amount along x' to bring $\{O'\}$ back to the neutral axis and finally rotate $-\theta_i$ about z' to preserve the orientation. The resulting HTM is given by

$$\begin{aligned} \mathbf{T}_i^c(\xi_i, q_i) &= \mathbf{R}_z(\theta_i) \mathbf{P}_x(\lambda_i) \mathbf{R}_y(\xi_i \phi_i) \mathbf{P}_x(-\lambda_i) \mathbf{R}_z(-\theta_i) \\ &= \begin{bmatrix} \mathbf{R}_i^c(\xi_i, q_i) & \mathbf{p}_i^c(\xi_i, q_i) \\ \mathbf{0}_{1 \times 3} & 1 \end{bmatrix}, \end{aligned} \quad (\text{A.14})$$

where $\mathbf{R}_z \in SO(2)$, $\mathbf{R}_y \in SO(2)$ are homogeneous rotational matrices about the Z and Y axes given by equations (A.15) and (A.16), $\mathbf{P}_x \in \mathbb{R}$ is the homogeneous translation matrix along the X axis given by equation (A.17). $\mathbf{R}_i^c \in SO(3)$ and $\mathbf{p}_i^c \in \mathbb{R}^3$ are the rotational and translation components of the HTM respectively

$$\mathbf{R}_z(\varsigma) = \begin{bmatrix} \cos \varsigma & -\sin \varsigma & 0 & 0 \\ \sin \varsigma & \cos \varsigma & 0 & 0 \\ 0 & 0 & 1 & 0 \\ 0 & 0 & 0 & 1 \end{bmatrix} \quad (\text{A.15})$$

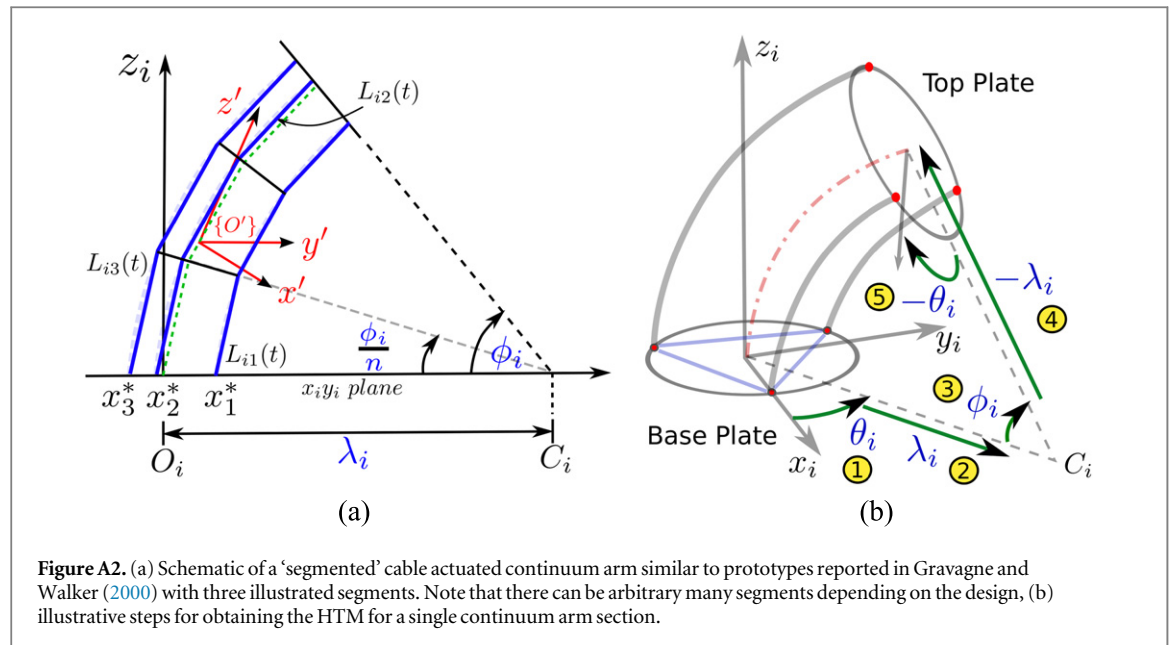


Figure A2. (a) Schematic of a 'segmented' cable actuated continuum arm similar to prototypes reported in Gravagne and Walker (2000) with three illustrated segments. Note that there can be arbitrary many segments depending on the design, (b) illustrative steps for obtaining the HTM for a single continuum arm section.

$$\mathbf{R}_y(\zeta) = \begin{bmatrix} \cos \zeta & 0 & \sin \zeta & 0 \\ 0 & 1 & 0 & 0 \\ -\sin \zeta & 0 & \cos \zeta & 0 \\ 0 & 0 & 0 & 1 \end{bmatrix} \quad (\text{A.16})$$

$$\mathbf{P}_x(\zeta) = \begin{bmatrix} 1 & 0 & 0 & \zeta \\ 0 & 1 & 0 & 0 \\ 0 & 0 & 1 & 0 \\ 0 & 0 & 0 & 1 \end{bmatrix}. \quad (\text{A.17})$$

References

- Adams R A and Essex C 2006 *Calculus: a complete course Sequences, Series, and Power Series* vol 6 (Reading, MA: Addison-Wesley)
- Bailly Y, Amirat Y and Fried G 2011 Modeling and control of a continuum style microrobot for endovascular surgery *IEEE Trans. Robot.* **27** 1024–30
- Braganza D, Dawson D M, Walker I D and Nath N 2006 Neural network grasping controller for continuum robots *IEEE Conf. Decision and Control* **6445–9**
- Buckingham R 2002 Snake arm robots *Ind. Robot, Int. J.* **29** 242–5
- Burdick J W, Radford J and Chirikjian G S 1993 A sidewinding locomotion gait for hyper-redundant robots *Proc. IEEE Int. Conf. Robotics and Automation* pp 101–6
- Buss S R 2004 Introduction to inverse kinematics with Jacobian transpose, pseudoinverse and damped least squares methods (San Diego, CA: University of California) (<http://math.ucsd.edu/~sbuss/ResearchWeb/ikmethods/iksurvey.pdf>)
- Caldwell D G, Medrano-Cerda G A and Goodwin M 1995 Control of pneumatic muscle actuators *IEEE Control Syst. Mag.* **15** 40–48
- Chirikjian G S 1994 Hyper-redundant manipulator dynamics: a continuum approximation *Adv. Robot.* **9** 217–43
- Chirikjian G S and Burdick J W 1990 An obstacle avoidance algorithm for hyper-redundant manipulators *IEEE Int. Conf. Robotics and Automation* vol 1 pp 625–31
- Chirikjian G S and Burdick J W 1990 Kinematics of hyper-redundant manipulators *Proc. 2nd Int. Workshop on Advances in Robot Kinematics (Linz)* pp 392–9
- Chirikjian G S and Burdick J W 1994 A modal approach to hyper-redundant manipulator kinematics *IEEE Trans. Robot. Autom.* **10** 343–54
- Conrad B L, Jung J, Penning R S and Zinn M R 2013 Interleaved continuum-rigid manipulation: an augmented approach for robotic minimally-invasive flexible catheter-based procedures *IEEE Int. Conf. Robotics and Automation* pp 718–24
- Dasgupta B and Choudhury P 1999 A general strategy based on the Newton–Euler approach for the dynamic formulation of parallel manipulators *Mech. Mach. Theory* **34** 801–24
- Davies J B C, Lane D M, Robinson G C, O'Brien D J, Pickett M, Sfakiotakis M and Deacon B 1998 Subsea applications of continuum robots *Proc. Int. Underwater Technology Symp. (April 1998)* pp 363–9
- Featherstone R 2008 *Rigid Body Dynamics Algorithms* vol 49 (Berlin: Springer)
- Giri N and Walker I D 2011 Three module lumped element model of a continuum arm section *IEEE/RSJ Int. Conf. Intelligent Robots and Systems* pp 4060–5
- Godage I S, Branson D T, Guglielmino E and Caldwell D G 2012 Path planning for multisection continuum arms *IEEE Int. Conf. Mechatronics and Automation* pp 1208–13
- Godage I S, Nanayakkara T and Caldwell D G 2012 Locomotion with continuum limbs *IEEE/RSJ Int. Conf. Intelligent Robots and Systems (IROS)* pp 293–8
- Gravagne I A and Walker I D 2000 On the kinematics of remotely-actuated continuum robots *IEEE Int. Conf. Robotics and Automation* pp 2544–50
- Grissom M D, Chitrakaran V, Dienno D, Csencits M, Pritts M, Jones B, McMahan W, Dawson D, Rahn C and Walker I D 2006 Design and experimental testing of the octarm soft robot manipulator *Defense and Security Symp. (International Society for Optics and Photonics, 2006)* 62301F–62301F
- Jones B A and Walker I D 2006 Kinematics for multisection continuum robots *IEEE Trans. Robot.* **22** 43–55
- Jones B A and Walker I D 2007 Limiting-case analysis of continuum trunk kinematics *IEEE Int. Conf. Robotics and Automation* pp 1363–8
- Kapadia A D, Walker I D, Dawson D M and Tatlicioglu E 2010 A model-based sliding mode controller for extensible continuum robots *Proc. 9th WSEAS Int. Conf. Signal Processing, Robotics and Automation* pp 113–20
- Laschi C, Cianchetti M, Mazzolai B, Margheri L, Follador M and Dario P 2012 Soft robot arm inspired by the octopus *Adv. Robot.* **26** 709–27
- Li J and Xiao J 2011 Determining 'grasping' configurations for a spatial continuum manipulator *IEEE/RSJ Int. Conf. Robots and Systems* pp 4207–14
- Mahl T, Hildebrandt A and Sawodny O 2012 Forward kinematics of a compliant pneumatically actuated redundant

- manipulator *IEEE Conf. Industrial Electronics and Applications* pp 1267–73
- Maplesoft 2009 *Maple User Manual*
- Mazzolai B, Margheri L, Cianchetti M, Dario P and Laschi C 2012 Soft-robotic arm inspired by the octopus: II. From artificial requirements to innovative technological solutions *Bioinspiration Biomimetics* **7** 025005
- McMahan W, Chitrakaran V, Csencsits M A, Dawson D M, Walker I D, Jones B A, Pritts M B, Dienno D, Grissom M and Rahn C D 2006 Field trials and testing of the octarm continuum manipulator *IEEE Int. Conf. Robotics and Automation* pp 2336–41
- Mochiyama H 2006 Hyper-flexible robotic manipulators *IEEE Int. Symp. Micro-Nano Mechatronics and Human Science* pp 41–46
- Murray R M, Li Z and Sastry S S 1994 *A Mathematical Introduction to Robotic Manipulation* (Boca Raton, FL: CRC Press)
- Neppalli S, Csencsits M A, Jones B A and Walker I D 2009 Closed-form inverse kinematics for continuum manipulators *Adv. Robot.* **23** 2077–91
- Robinson G and Davies J B C 1999 Continuum robots—a state of the art *IEEE Int. Conf. Robotics and Automation* pp 2849–54
- Rolf M and Steil J J 2012 Constant curvature continuum kinematics as fast approximate model for the bionic handling assistant *IEEE/RSJ Int. Conf. Intelligent Robots and Systems* pp 3440–6
- Salisbury K 1988 Whole arm manipulation *Proc. 4th Int. Symp. Robotics Research* (Cambridge, MA: MIT Press) pp 183–9
- Selig J M 1992 *Introductory Robotics* vol 5 (Saddle River, NJ: Prentice Hall)
- Seok S, Onal C D, Cho K-J, Wood R J, Rus D and Kim S 2013 Meshworm: a peristaltic soft robot with antagonistic nickel titanium coil actuators *IEEE/ASME Trans. Mechatronics* **18** 1485–97
- Shabana A A 1998 Computer implementation of the absolute nodal coordinate formulation for flexible multibody dynamics *Nonlinear Dyn.* **16** 293–306
- Shabana A A 2005 *Dynamics of Multibody Systems* (Cambridge: Cambridge University Press)
- Siciliano B and Khatib O 2008 *Springer Handbook of Robotics* (New York: Springer)
- Simaan N, Taylor R and Flint P 2004 A dexterous system for laryngeal surgery *IEEE Int. Conf. Robotics and Automation* pp 351–7
- Stein W A et al 2012 *Sage Mathematics Software (Version 4.8.0)* The Sage Development Team URL (<http://www.sagemath.org>)
- Suzumori K 1996 Elastic materials producing compliant robots *Robot. Auton. Syst.* **18** 135–40
- Tatlicioglu E, Walker I D and Dawson D M 2007 Dynamic modelling for planar extensible continuum robot manipulators *IEEE Int. Conf. Robotics and Automation* pp 1357–62
- Trivedi D, Rahn C D, Kier W M and Walker I D 2008 Soft robotics: biological inspiration, state of the art, and future research *Appl. Bionics Biomech.* **5** 99–117
- Walker I D 2007 Some issues in creating ‘invertebrate’ robots *Relation* **10** 4586
- Walker I D 2013 Continuous backbone ‘continuum’ robot manipulators *ISRN Robot.* **2013** 1–19
- Walker I D, Carreras C, McDonnell R and Grimes G 2006 Extension versus bending for continuum robots *Int. J. Adv. Robot. Syst.* **3** 1729–8806
- Xu K and Simaan N 2010 Analytic formulation for kinematics, statics, and shape restoration of multibackbone continuum robots via elliptic integrals *J. Mech.* **2** 011006
- Zheng T, Branson D T, Kang R, Cianchetti M, Guglielmino E, Follador M, Medrano-Cerda G A, Godage I S and Caldwell D G 2012 Dynamic continuum arm model for use with underwater robotic manipulators inspired by octopus vulgaris *IEEE Int. Conf. Robotics and Automation* pp 5289–94
- Zheng T, Godage I S, Branson D T, Kang R, Guglielmino E, Medrano-Cerda G A and Caldwell D G 2013 Octopus inspired walking robot: design, control and experimental validation *IEEE Int. Conf. Robotics and Automation* pp 816–21